CHEMISTRY
A EUROPEAN JOURNAL

DOI: 10.1002/chem.200700560

Rational Tuning of Melting Entropies for Designing Luminescent Lanthanide-Containing Thermotropic Liquid Crystals at Room Temperature

Aude Escande,[a] Laure Guénée,[a] Homayoun Nozary,[a] Gérald Bernardinelli,[b] Frédéric Gumy,[c] Annina Aebischer,[c] Jean-Claude G. Bünzli,[c] Bertrand Donnio,[d] Daniel Guillon,[d] and Claude Piguet*[a]

Abstract: The connection of twelve peripheral and divergent dodecyloxy chains to a central tridentate aromatic binding unit provides the dodecacatenar ligand **L11**, for which room-temperature mesomorphism is detected. An enthalpically unbalanced large melting entropy ($\Delta S_m^{L11} = 226\ J\,mol^{-1}\,K^{-1}$) results from the programmed microsegregation induced in the crystalline phase, a phenomenon which is maintained in the associated lanthanide complexes $[Ln(\mathbf{L11})(NO_3)_3]$ and $[Ln(\mathbf{L11})(CF_3CO_2)_3]_2$. Low-temperature melting processes ($-43 \le T_m \le -25\,°C$) producing room-temperature hexagonal columnar liquid-crystalline phases thus result for these novel lanthanidomesogens. A combined photophysical (high-resolution emission spectroscopy), thermodynamic (differential scanning calorimetry, DSC) and structural (small-angle X-ray diffraction, SA-XRD) investigation of the melting process shows minor structural changes occurring between the crystal (Cr) and the hexagonal columnar mesophase (Col_h) in the complexes, which allows the assignment of the existence of these unusual first-order phase transitions to the negligible mixing entropy produced by the two viscous phases at low temperature. Extension of the concept of chemical tuning of melting entropies for the global design of room-temperature metallomesogens and liquid crystals is discussed.

Keywords: entropy · lanthanides · liquid crystals · metallomesogens · phase transitions

Introduction

Up to the turn of the 20th century, thermotropic lanthanidomesogens, that is, lanthanide-containing liquid crystals, remained a curiosity, despite potential attractive technological applications for improving brightness, view-angle and color quality in flat liquid-crystal displays.[1] Pioneering research efforts indeed focussed on two well-identified classes of complexes that incorporated trivalent lanthanides, Ln^{III}, and exhibited thermotropic liquid crystalline properties. 1) Neutral disk-like sandwich complexes $[Ln(\mathbf{Li}\text{-}2H)_2]$ ($\boldsymbol{i} = 1$–5, as shown)[2] or triple-decker complexes $[Ce_2(Porphyrin)_3]$[3] have been shown to stack on top of each other to produce hexagonal columnar mesophases (Col_h) in the 20–250 °C range, whereas; 2) lanthanide size-dependent lamellar organizations (usually smectic A, SmA) have been established to be common for the rod-like complexes $[Ln(\mathbf{Li}\text{-}H)_3X_3]$ ($\boldsymbol{i} = 6$–8; X = NO_3, $H_{25}C_{12}OSO_3$, Cl, β-diketonate).[4] The intense scientific activity dedicated to this topic has been thoroughly reviewed in 2002 by Binnemans and Görller-Walrand,[1] who have significantly contributed to the rapid evolution of thermotropic lanthanidomesogens during the past four years with: 1) the preparation of the first d–f heterome-

[a] A. Escande, Dr. L. Guénée, Dr. H. Nozary, Prof. Dr. C. Piguet
Department of Inorganic, Analytical and Applied Chemistry
University of Geneva
30 quai E. Ansermet, –1211 Geneva 4 (Switzerland)
Fax: (+41) 22-379-6830
E-mail: Claude.Piguet@chiam.unige.ch

[b] Dr. G. Bernardinelli
Laboratory of X-ray Crystallography, University of Geneva
24 quai E. Ansermet, 1211 Geneva 4 (Switzerland)

[c] F. Gumy, Dr. A. Aebischer, Prof. Dr. J.-C. G. Bünzli
Laboratory of Lanthanide Supramolecular Chemistry
École Polytechnique Fédérale de Lausanne
BCH 1402 1015 Lausanne (Switzerland)

[d] Dr. B. Donnio, Dr. D. Guillon
Institut de Physique et Chimie des Matériaux de Strasbourg-IPCMS
CNRS-ULP UMR 7504, 23 rue du Loess
B.P. 43 67034 Strasbourg Cedex 2 (France)

Supporting information for this article is available on the WWW under http://www.chemeurj.org/ or from the author and includes the experimental section, as well as the associated analytical data. Additional tables (Tables S1–S6) and figures (Figure S1–S14) for structural and spectroscopic analyses and crystallographic data for compound **18**.

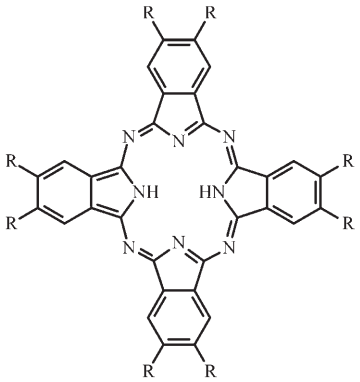

R = C_nH_{2n+1} : **L1**
R = $CH_2OC_nH_{2n+1}$: **L2**
R = OC_nH_{2n+1} : **L3**
R = SC_nH_{2n+1} : **L4**
R = $(OCH_2CH_2)_nCH_3$: **L5**

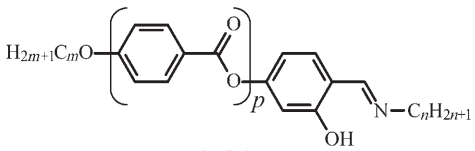

p = 0 : **L6**
p = 1 : **L7**
p = 2 : **L8**

tallic metallomesogens;[5] 2) the isolation of the first binuclear f–f lanthanidomesogens;[6] 3) the observation of the first nematic lanthanidomesogens[7] and; 4) the introduction of block 5f metals in standard liquid crystalline phases[8] (i.e., actinidomesogens).[9] In a parallel effort, we have proposed a simplistic thermodynamic approach for rationalizing the molecular design of lanthanidomesogens.[10] According to this qualitative model, a thermotropic liquid crystalline phase results from the melting of a microsegregated solid, in which the packed polarizable cores of the molecules are grafted with long, flexible and poorly polarizable alkyl chains filling the voids in the crystals. At the phase transition, the melting temperature, $T_m = \Delta H_m/\Delta S_m$, mainly reflects the behavior of the flexible alkyl chains, for which an endothermic enthalpy change characterizes the loss of correlation of the weakly cohesive interactions involving the alkyl chains (−4 kJ/methylene unit, $\Delta H_m > 0$).[11] On the other hand, a large entropic gain results from the relaxation of the usually all-*trans* conformations of the alkyl chains found in the solid state, which eventually leads to a characteristic disordered molten state in the mesophase ($\Delta S_m > 0$).[12] It is worth noting that ΔH_m also includes some contributions arising from the partial loss of correlation of the rigid cores occurring during the melting process, and which is responsible for the fluidity of the mesophase. In a rough approximation, the mesophase can be thus considered as made up of residual clusters of interacting molecules dispersed in a liquid continuum provided by the molten alkyl chains. This simple model thus predicts that the enthalpic and entropic contributions to the melting process leading to the thermotropic liquid crystalline phase indeed mirror those encountered during the simple melting of hydrocarbons, and for which remarkable and precise trends have been established. 1) A reduction of the intermolecular interactions between the alkyl chains occurs at the melting point, which corresponds to a change in dynamics between the two states (measured by $\Delta S_m > 0$) that is primarily correlated with the reduction in bonding between the two states (measured by $\Delta H_m > 0$).[12] 2) A relatively large increase in motion on melting alkyl chains correlates with a relatively large decrease in bonding (enthalpy/entropy compensation). 3) Exact enthalpy/entropy compensation (i.e., an invariant temperature of melting $T_m = \Delta H_m/\Delta S_m$) has been recently reported for phase transitions between layered crystalline organizations and hexagonal columnar mesophases in silver-alkanethiolate, whatever the length of the alkyl chains.[11] However, such strict compensation effects are rare and they imply that the well depth of the energy potential of the interaction (controlling ΔH_m) is strictly correlated with the force constant of the association process (controlling ΔS_m), thus leading to systematic variations in the same direction.[12,13] The latter behavior is observed when minor molecular and structural changes occur within a family of microscopic objects, and it produces only minor variations of the temperatures of melting, a common observation in liquid crystals whereby the systematic variation of alkyl chain lengths generally poorly affects the melting temperature within an isostructural series. However, large structural variations have no reasons to follow this trend in $\Delta H_m/\Delta S_m$ compensation,[13] and, for instance, a large number of flexible alkyl chains in a polycatenar ligand is expected to drastically increase ΔS_m because of the large number of noncorrelated internal rotors gaining degrees of freedom upon melting.[12] On the other hand, the spread of the alkyl chains in polycatenar ligands is not favorable for a large increase in the intermolecular cohesion between the chains, and we can reasonably expect that ΔH_m increases much slower than ΔS_m for these systems, thus drastically reducing temperatures of melting and possibly producing room-temperature metallomesogens. Finally, the domain of existence of a mesophase is limited at high temperature by the clearing process occurring at T_c, which leads to the liquid phase. The clearing temperature $T_c = \Delta H_c/\Delta S_c$ essentially concerns the polarizable cores, whereby ΔH_c reflects the breakdown of the cohesion of the residual organized polarizable clusters and ΔS_c measures the moderate increase in motion on melting these rigid clusters.[10] In this context, we have recently shown how some judicious alternation of the polarization of the rigid aromatic rings within the rigid cores may affect ΔH_c, and induce T_c to be large enough to ensure the existence of a liquid crystalline state.[14] Interestingly, our rough qualitative approach had some successes in fairly explaining; 1) the high-temperature mesomorphism of the bicatenar ligand **L9** ($Cr \xrightarrow{144\,^\circ C} SmA$, $\Delta H_m^{L9} = 28\ kJ\,mol^{-1}$ and $\Delta S_m^{L9} = 66\ J\,mol^{-1}K^{-1}$), because of the very limited number of divergent alkoxy chains;[15] 2) the removal of liquid crystalline properties in the associated complexes $[Ln(\mathbf{L9})(NO_3)_3]$ and $[Ln(\mathbf{L9})(CF_3CO_2)_3]_2$, resulting from the coordination of bulky LnX_3 units, which hamper intermolecular cohesion between the polarizable cores, thus decreasing ΔH_c and T_c,[15–17] and; 3) the restoration of the mesomorphism in the hexacatenar complexes $[Ln(\mathbf{L10})(NO_3)_3]$ and $[Ln(\mathbf{L10})(CF_3CO_2)_3]_2$, because the grafting of six divergent flexible

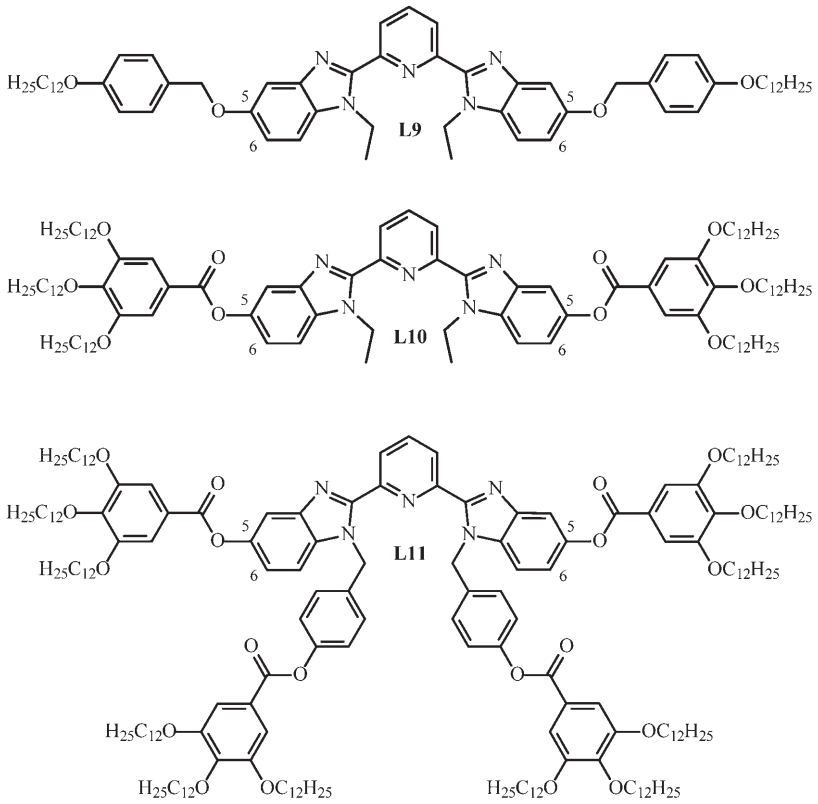

alkoxy chains to the rigid core in **L10** (instead of only two in **L9**) decreases T_m to such an extent that $T_m < T_c$, despite the small values of ΔH_c and T_c.[18,19] The major criticism about our thermodynamic model results from our failure to support its predictions concerning enthalpic and entropic contributions with some quantitative determination of ΔS_m and ΔH_c.[10] Indeed, the family of ligands and complexes derived from **L9** and **L10** systematically displayed glassy or second-order phase transitions for the melting processes and decomposed quickly at high temperature when entering the isotropic liquid.[14–19] These characteristics severely limit any reliable determination of the thermodynamic parameters controlling the phase transitions. Herein, we address this limiting point by designing a novel dodecacatenar ligand **L11** and its lanthanide complexes, which are able: 1) to produce entropically-driven low-temperature melting processes, in complete agreement with the predicting model, and; 2) to systematically exhibit first-order phase transitions with easily accessible thermodynamic parameters.

Results and Discussion

Synthesis, characterization, and properties of the ligand L11 and of its lanthanide complexes [Ln(L11)(NO$_3$)$_3$] (Ln = La–Lu) and [Eu(L11)(CF$_3$CO$_2$)$_3$]$_2$ in the solid state: As previously discussed in the introduction, the increasing number of divergent flexible alkyl chains in the polycatenar ligand in going from **L9** ($n=2$) to **L10** ($n=6$) significantly reduces the melting temperature by $\Delta T_m = 119\,°C$, a phenomenon tentatively assigned to a large and enthalpically unbalanced increase of ΔS_m.[10] To further exploit this effect, six additional peripheral dodecyloxy chains have been connected to the central tridentate 2,6-bis-(benzimidazol-2-yl)pyridine binding unit in the target ligand **L11**. The commercially available 4-methoxybenzyl alcohol (**1**) is first brominated, then coupled with primary 2-nitroareneamine to give the required secondary *o*-nitroareneamine **2**. A double amidation reaction with pyridine-2,6-diacylchloride leads to the bis-*ortho*-nitroamide precursor **3**, which eventually undergoes a double-reductive Philips reaction to give the polyaromatic core **4**. The simultaneous deprotection of the four methoxy groups with boron tribromide provides the poorly soluble tetrol **5**, which is eventually substituted with four lipophilic gallic acid residues in order to give the dodecacatenar ligand **L11** (global yield = 26% from **1**, Scheme 1). Alternatively, the grafting of the tetrol **5** with four 4-ethoxy-benzoic acid units produces the less lipophilic ligand **L12**, which has been used for structural investigations.

Stoichiometric mixing of **L11** or **L12** with Ln(NO$_3$)$_3$·xH$_2$O (Ln = La–Lu, $x=2$–4) or Eu(CF$_3$CO$_2$)$_3$·3H$_2$O in acetonitrile/dichloromethane yields 63–88% of [Ln(**L11**)(NO$_3$)$_3$]·xH$_2$O (Ln = La, $x=1.6$: **6**; Ln = Pr, $x=0.5$: **7**; Ln = Sm, $x=1.8$: **8**; Ln = Eu, $x=1.6$: **9**; Ln = Gd, $x=1.0$: **10**; Ln = Tb, $x=0$: **11**; Ln = Tm, $x=0$: **12**; Ln = Yb, $x=0$: **13**; Ln = Lu, $x=0$: **14**; Ln = Y, $x=0$: **15**) [Eu(**L11**)(CF$_3$CO$_2$)$_3$] (**16**), and [Eu(**L12**)(CF$_3$CO$_2$)$_3$]·3.9H$_2$O (**17**, elemental analyses are collected in Table S1 in the Supporting Information, and water contents were confirmed by TGA analyses). The observation of the three characteristic infrared-active NO vibrations of C_{2v}-symmetrical nitrate anions ($\nu_1(A_1) = 1470$–$1490\ cm^{-1}$, $\nu_5(B_2) = 1288$–$1295\ cm^{-1}$, $\nu_2(A_1) = 1028$–$1035\ cm^{-1}$) implies the direct binding of the anions to the metal (Table S2 in the Supporting Information).[20] The large differences ν_1–$\nu_5 = 200$–$210\ cm^{-1}$ strongly suggest a systematic bidentate binding mode toward Ln^{III}, as previously established by X-ray diffraction studies for the analogous complexes [Ln(**L10**)(NO$_3$)$_3$].[18] For [Eu(**L11**)(CF$_3$CO$_2$)$_3$], the typical CO$_2$ stretching vibration of the anion occurs at $1679\ cm^{-1}$. We were however unable to grow monocrystals for the complexes **6**–**17** or for the less lipophilic analogues [Ln(**L12**)(NO$_3$)$_3$], but [Lu(**L12**)(CF$_3$CO$_2$)$_3$]·0.5H$_2$O (**18**)

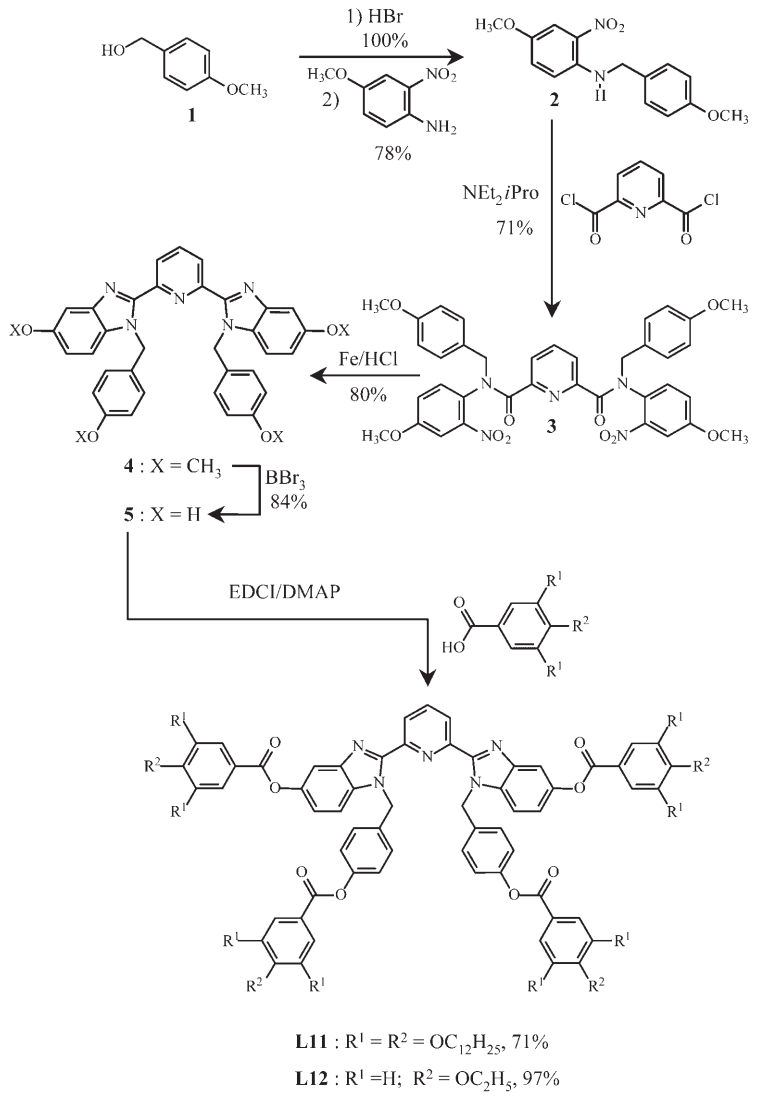

Scheme 1. Synthesis of the ligands **L11** and **L12**.

crystallizes upon slow evaporation of a concentrated dichloromethane solution to give colorless prisms suitable for an X-ray diffraction investigation. The crystal structure of **18** shows the existence of centrosymmetrical doubly-bridged dimers $[Lu(\mathbf{L12})(CF_3CO_2)_3]_2$, together with one interstitial water molecule per dimer (Figure 1). Although the formation of CF_3CO_2-bridged dimeric complexes obtained with isomeric coordinated I-shaped 6,6′-disubstituted ligands in $[Lu(\mathbf{L13})(CF_3CO_2)_3]_2$ (two bridging anions, Lu···Lu = 5.067(1) Å),[16] $[Lu(\mathbf{L14})(CF_3CO_2)_3]_2$ (two bridging anions, Lu···Lu = 5.7170(5) Å),[19] and $[Lu(\mathbf{L15})(CF_3CO_2)_3(OH_2)]_2$ (no bridging anion, Lu···Lu = 6.2859(5) Å)[17] is well-established, there is only one previous crystal structure describing the formation of a related dimer with the alternative coordinated V-shape 5,5′-disubstituted ligand **L10** in $[La(\mathbf{L10})(CF_3CO_2)_3]_2$ (four bridging anions, La···La = 4.7955(8) Å, see Figure S1 in the Supporting Information).[19] The reluctance of the 5,5′-disubstituted ligands to produce dimeric CF_3CO_2-bridged lanthanide complexes can be traced back to the sterical constraint resulting from the head-to-head dimerization of two V-shaped complexes, for which the extended semirigid peripheral aromatic side arms point against each other. For $[La(\mathbf{L10})(CF_3CO_2)_3]_2$, a strong deviation of La^{III} out of the chelating N1, N2, N4 plane (deviation of 1.03(1) Å toward the second metal) combined with a parallel, but shifted, face-to-face arrangement of the tridentate binding unit are required in order to offer sufficient access for forming four intermetallic trifluoacetate bridges (see Figure S1 in the Supporting Information).[19] For $[Lu(\mathbf{L12})(CF_3CO_2)_3]_2$, similar geometrical characteristics are observed with a shifted face-to-face arrangement of the pseudoplanar tridentate binding units (pyridine-benzimidazole dihedral angles = 12.0 and 17.1°, Table S4 in the Supporting Information), and a smaller deviation of Lu^{III} out of the chelating N1, N2, N4 plane (0.402(7) Å, Figure 1b). The Lu–N (average 2.43(5) Å) and Lu–O (average 2.32(2) Å, Table S3 in the Supporting Information) bond lengths are standard, and we calculate an ionic radius $R_{Lu}^{CN=8} = 0.968$ Å in $[Lu(\mathbf{L12})(CF_3CO_2)_3]_2$ by using Shannon's definition with $r(N) = 1.46$ Å and $r(O) = 1.35$ Å, which fairly matches 0.977 Å expected for eight-coordinate Lu^{III}.[21]

The Lu···Lu distance = 5.4443(5) Å in $[Lu(\mathbf{L12})(CF_3CO_2)_3]_2$ lies within the 5.0–5.7 Å range spanned by the previously reported $\{Lu(CF_3CO_2)_2Lu\}$ structural motives,[16,17,19] and the rigid polyaromatic core of the complex can be roughly inserted within a disk with 27 Å diameter (Figure 2). Finally, each asymmetric unit in the crystal structure of **18** is involved in six intermolecular π–π stacking interactions, but none of them occurs within the same dimeric unit (Figure S2, Supporting Information).

Further insight into the molecular organization in the solid state may be gained by optical spectroscopy. The absorption spectra of the ligand **L11** and of its complexes $[Ln(\mathbf{L11})(NO_3)_3]$ (**6–15**), $[Eu(\mathbf{L11})(CF_3CO_2)_3]$ (**16**), and $[Eu(\mathbf{L12})(CF_3CO_2)_3]$ (**17**) in the solid state and in solution are dominated by intense ligand-centered π→π* transitions in the UV domain (28000–40000 cm^{-1}, see Figure S3 in the

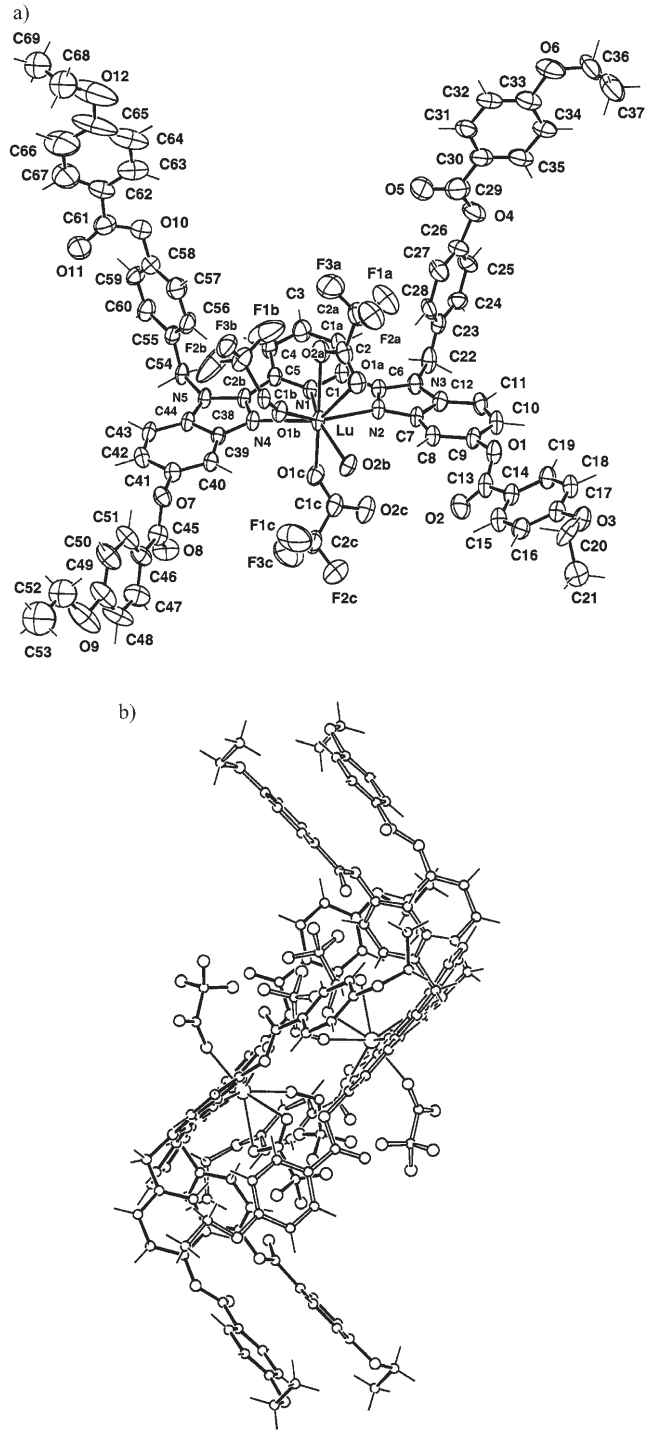

Figure 1. Perspective views of $[Lu(\mathbf{L12})(CF_3CO_2)_3]_2$ in the crystal structure of **18**. a) Representation of the asymmetric unit with numbering scheme (ellipsoids are represented at the 40% probability level). b) View of the centrosymmetrical dimer perpendicular to the Lu···Lu direction.

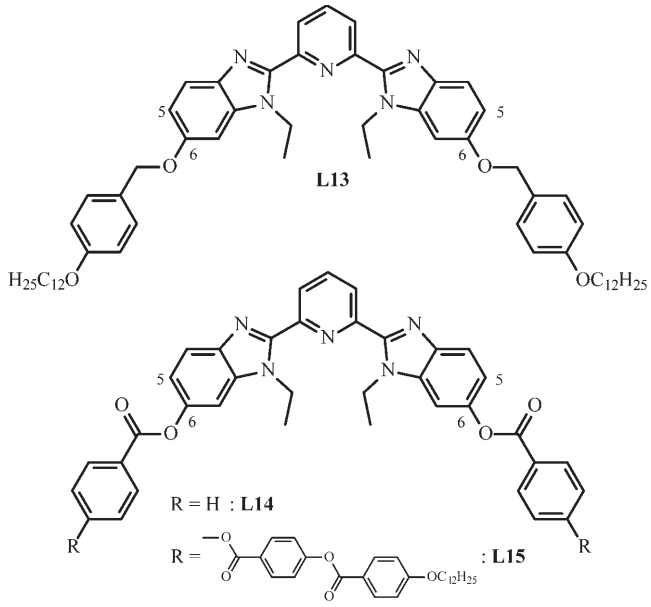

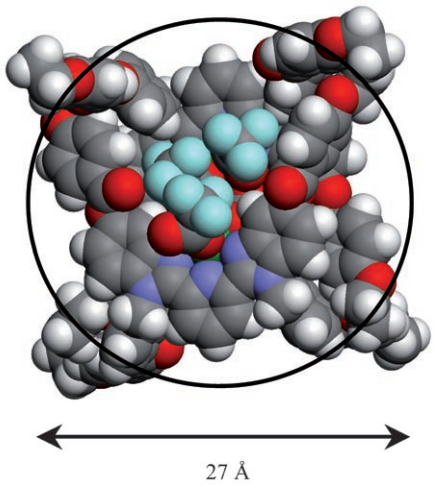

Figure 2. CPK view of the dimer $[Lu(\mathbf{L12})(CF_3CO_2)_3]_2$ perpendicular to the N1, N2, N4 plane and showing the pseudocircular projection of the rigid core.

Supporting Information). Upon complexation of **L11** to $Ln(NO_3)_3$, the low-energy absorption side band is systematically red-shifted by about 3000 cm^{-1}, which is diagnostic for the *trans–trans→cis–cis* conformational change of the tridentate binding unit accompanying the coordination of the metal (see Figure S3 in the Supporting Information).[22] Excitation of **L11**($\pi\rightarrow\pi^*$) produces a poorly structured, short-lived, and broad emission covering the 24250–18200 cm^{-1} range and originating from both $^1\pi\pi^*$ and $^3\pi\pi^*$ states (Table 1). Upon complexation to Lu^{III} in $[Lu(\mathbf{L11})(NO_3)_3]$ (**14**), the rigidification of the ligand combined with the Lu heavy-atom effect concomitantly improve the feeding ($^1\pi\pi^*\rightarrow{}^3\pi\pi^*$ intersystem crossing, ISC) and the radiative deexcitation of the ligand-centered $^3\pi\pi^*$ level, thus providing an easily detectable long-lived emission at 20800 cm^{-1} (0–0 phonon, $\tau(^3\pi\pi^*) = 37.3(7)$ ms at 77 K, Table 1). When Lu^{III} is replaced with Gd^{III} in $[Gd(\mathbf{L11})(NO_3)_3]$ (**10**), a very similar emission spectrum is observed (Figure 3a), except for the larger intensity and shorter lifetime of the ligand-centered $^3\pi\pi^*$ state

Table 1. Absorption and emission properties of ligand **L11** and of its complexes [Ln(**L11**)$(NO_3)_3$] (Ln = Eu, Gd, Tb, Lu).

Compound	Ligand-centered					Metal-centered	
	Absorption [cm^{-1}][a] $\pi\rightarrow\pi^*$	ε [$M^{-1}\,cm^{-1}$]	Emission [cm^{-1}][b] $^1\pi\pi^*$	Emission [cm^{-1}] $^3\pi\pi^*$	Lifetime [ms] τ ($^3\pi\pi^*$)	Emission [cm^{-1}]	Lifetime [ms]
L11	35710	77700	24250 br	18200 br	<0.01		
	32570 sh	55400			77–295 K		
	30670 sh	44310					
[Lu(**L11**)$(NO_3)_3$] (**13**)	35590	68600	24300	20800 sh	0.78(2) 295 K		
	32890 sh	54650		18860			
	27320	31190		17670 sh	37.3(7) 77 K		
				16230 sh			
[Gd(**L11**)$(NO_3)_3$] (**10**)	35560	69200	25060	20325 sh	<0.01 295 K		
	32840 sh	54600		19050	1.91(1) 77 K		
	27800	24570		17890			
				16750			
[Eu(**L11**)$(NO_3)_3$] (**9**)	35460	70700	[c]	[c]		18904 $^5D_1\rightarrow{}^7F_0$	
	33000 sh	55280				18553 $^5D_1\rightarrow{}^7F_1$	
	27780	24860				17921 $^5D_1\rightarrow{}^7F_2$	
						17036 $^5D_0\rightarrow{}^7F_0$	Eu($^5D_0$):
						16750 $^5D_0\rightarrow{}^7F_1$	1.15(1) 295 K
						16155 $^5D_0\rightarrow{}^7F_2$	1.29(1) 77 K
						15337 $^5D_0\rightarrow{}^7F_3$	1.27(6) 10 K
						14556 $^5D_0\rightarrow{}^7F_4$	
[Tb(**L11**)$(NO_3)_3$] (**11**)	35460	68780	[c]	18900	[d]	20284 $^5D_4\rightarrow{}^7F_6$	Tb($^5D_4$):
	32680 sh	52320				18265 $^5D_4\rightarrow{}^7F_5$	0.10 (1) 295 K
	27540	24860				16978 $^5D_4\rightarrow{}^7F_4$	1.07(4) 77 K
						16026 $^5D_4\rightarrow{}^7F_3$	
						15333 $^5D_4\rightarrow{}^7F_2$	
						14937 $^5D_4\rightarrow{}^7F_1$	
						14728 $^5D_4\rightarrow{}^7F_0$	

[a] Absorption spectra recorded for 10^{-4} M solution in CH_2Cl_2 at 295 K, sh: shoulder. [b] Emission spectra recorded from solid-state samples. [c] Ligand-centered luminescence quenched by transfer to Ln ion. [d] The intensity is too weak to obtain reliable lifetime measurements.

(0–0 phonon: 20325 cm^{-1}, $\tau(^3\pi\pi^*)=1.91(1)$ ms at 77 K, Table 1), resulting from the additional electrostatic interactions involving the ligand-centered singlet and triplet excited states, and the paramagnetic Gd($^8S_{7/2}$) ground state.[23]

Upon complexation of Tb^{III} in [Tb(**L11**)$(NO_3)_3$] (**11**, Figure 3b) or Eu^{III} in [Eu(**L11**)$(NO_3)_3$] (**9**, Figure 3c), efficient **L11**$\rightarrow Ln^{III}$ energy transfers occur, thus leading to the detection of the well-established metal-centered luminescence arising from Tb($^5D_4$), Eu($^5D_1$), and Eu($^5D_0$) excited levels (Table 1 and Figure 3). The roughly temperature-independent Eu($^5D_0$) lifetime in **9** (τ(Eu($^5D_0$)) = 1.15–1.30 ms, Table 1) is typical for Eu^{III} that is nine-coordinated by the three heterocyclic nitrogen atoms of the 2,6-bis(benzimidazol-yl)pyridine unit and by three bidentate nitrate anions as previously reported for [Eu(**L10**)$(NO_3)_3$] (τ(Eu($^5D_0$)) = 1.25–1.29 ms).[18] On the other hand, the drastic decrease of the Tb($^5D_0$) lifetime in going from 77 K to 295 K (1.07(4) and 0.10(1) ms, respectively), combined with the detection of some residual ligand-centered $^3\pi\pi^*$ emission above 77 K (Figure 3b), indicates the occurrence of the usual thermally activated $^3\pi\pi^*\leftarrow$Tb($^5D_4$) back transfer induced by the small energy gap $\Delta E = E(^3\pi\pi^*) - E(^5D_0) = 50$ cm^{-1} (Table 1).[20,24]

The high-resolution excitation profile of the nondegenerate Eu($^5D_0\leftarrow{}^7F_0$) transition in [Eu(**L11**)$(NO_3)_3$] (**9**) recorded at 10 K shows the existence of three different sites labelled I, II, and III (Figure 4a, Table 2 and Figure S4 in the Supporting Information). Laser-induced selective excitation of these sites provides very similar low-symmetrical spectra for sites I and III, but a slightly different pattern is observed for site II (Figure S5 in the Supporting Information). The same measurement performed on the well-established nine-coordinate monomer [Eu(**L10**)$(NO_3)_3$] in the solid and in the liquid crystalline states shows the exclusive existence of site III occurring at 17215 cm^{-1} (Figure 4b, Table 2).[18] Moreover, selective excitation of site III in [Eu(**L10**)$(NO_3)_3$] results in a crystal-field pattern similar to that observed upon selective excitation of the same site in [Eu(**L11**)$(NO_3)_3$] (see Figure S5 and S6 in the Supporting Information). We consequently assign site III to the nine-coordinate monomeric complex in the solid state. The closely related site I is characterized by a similar geometry, but with a 25% reduced lifetime and a 20 cm^{-1} blue-shifted Eu($^5D_0\leftarrow{}^7F_0$) transition (Table 2), which are diagnostic for partial interaction with extra water molecules in the first coordination sphere (as suggested by the elemental analysis). The application of the empirical Equation (1) of Frey and Horrocks[25] predicts $\bar{\nu}_{calcd} = 17245$ cm^{-1} for a Eu^{III} atom in [Eu(**L11**)$(NO_3)_3$-(OH_2)] coordinated by three heterocyclic nitrogen atoms ($\delta_{N\text{-heterocyclic}} = -15.3$ cm^{-1}),[26] six nitrate oxygen atoms ($\delta_{O\text{-nitrate}} = -13.3$ cm^{-1}),[25] and one water molecule ($\delta_{O\text{-water}} = -10.4$ cm^{-1})[25] at 295 K ($\bar{\nu}_0 = 17374$ cm^{-1} is the energy of the Eu($^5D_0\leftarrow{}^7F_0$) transition in the free ion, C_{CN} is an empirical coefficient depending on the coordination number (CN) of the metal, $C_{CN=8} = 1.06$, $C_{CN=9} = 1.0$, $C_{CN=10} = 0.95$ and δ_i

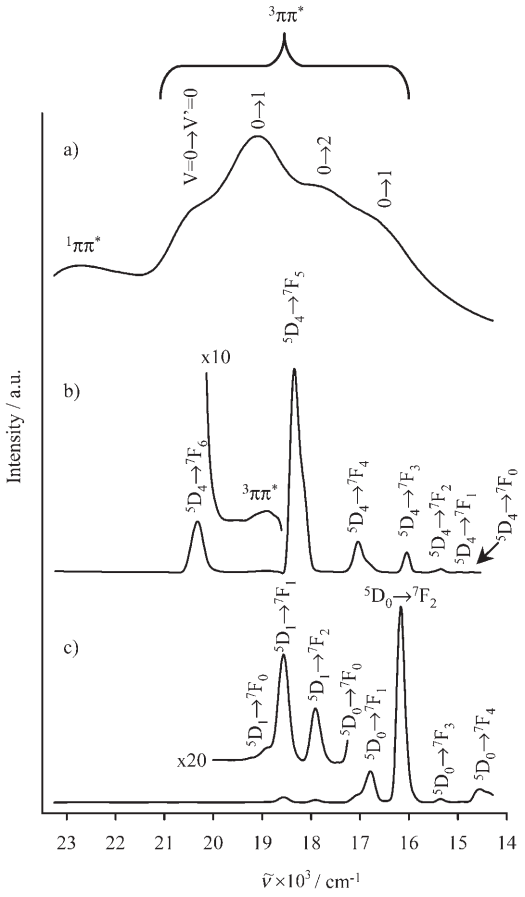

Figure 3. Steady-state emission spectra of a) [Gd(**L11**)$(NO_3)_3$] (**10**), b) [Tb(**L11**)$(NO_3)_3$] (**11**), and c) [Eu(**L11**)$(NO_3)_3$] (**9**) in the solid state at 77 K ($\bar{\nu}_{exc}=25\,125\ cm^{-1}$).

represents the nephelauxetic effect produced by an atom *i* bound to Eu^{III}).[25] Assuming the usual blue shift of 1 cm^{-1}/24 K for the Eu($^5D_0\leftarrow{}^7F_0$) transition,[27] we eventually obtain $\bar{\nu}_{calcd}=17\,233\ cm^{-1}$ for [Eu(**L11**)$(NO_3)_3(OH_2)$] at 10 K, a prediction in exact agreement with 17 233 cm^{-1} experimentally observed for the major site I in complex **9**.

$$\bar{\nu}_{calcd}=\bar{\nu}_0+C_{CN}\cdot\sum_{i=1}^{CN}\bar{\nu}_i\cdot\delta_i \qquad (1)$$

Finally, site II differs from site I by an 18 cm^{-1} blue-shift of the Eu($^5D_0\leftarrow{}^7F_0$) transition, whereas the Eu($^5D_0$) lifetime is diagnostic for a nonsolvated Eu^{III} (Table 2). These trends can be traced back to the formation of traces of the [Eu_2(**L11**)$_2(NO_3)_6$] dimer, in which each Eu^{III} is ten-coordinate by one tridentate ligand (three heterocyclic N atoms with $\delta_{N\text{-heterocyclic}}=-15.3\ cm^{-1}$), two bidentate nitrate anions (four nitrate oxygen atoms with $\delta_{O\text{-nitrate}}=-13.3\ cm^{-1}$) and two bridging nitrate anions (three bridging nitrate oxygen atoms with an unknown $\delta_{O\text{-bridging}}$ parameter), as previously established in the crystal structure of [Eu_2(**L14**)$_2(NO_3)_6$].[18] The application of Equation 1 for site II ($\bar{\nu}_{calcd}=17\,263\ cm^{-1}$ at 295 K, Table 2) gives $\delta_{O\text{-bridging}}=-5.1\ cm^{-1}$, which is compatible with a limited nephelauxetic parameter characterizing a bridging nitrate group, for which the three O atoms interact with Eu^{III} atoms.

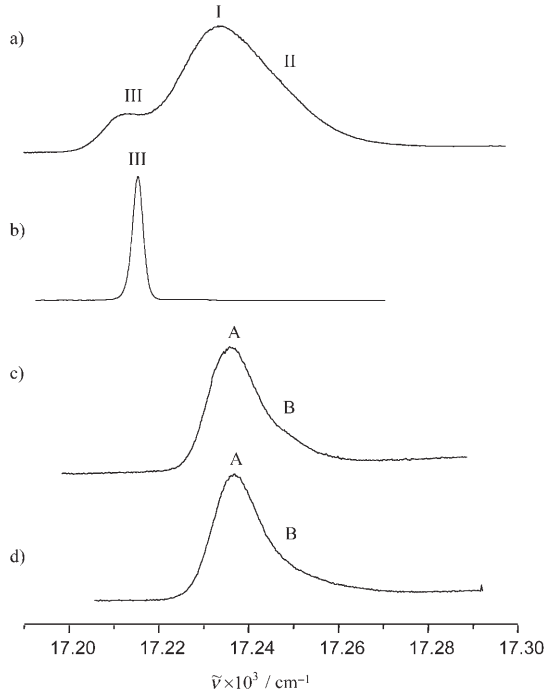

Figure 4. High-resolution excitation profiles of the Eu($^5D_0\leftarrow{}^7F_0$) transition in a) [Eu(**L11**)$(NO_3)_3$] (**9**), b) [Eu(**L10**)$(NO_3)_3$],[18] c) [Eu(**L11**)$(CF_3CO_2)_3$] (**16**), and d) [Eu(**L12**)$(CF_3CO_2)_3$] (**17**, solid state, 10 K).

Table 2. Maxima of the Eu($^5D_0\leftarrow{}^7F_0$) energy profiles in [Eu(**L11**)$(NO_3)_3$] (**9**), b) [Eu(**L10**)$(NO_3)_3$],[18] [Eu(**L11**)$(CF_3CO_2)_3$] (**16**), and [Eu(**L12**)$(CF_3CO_2)_3$] (**17**) at 10 K, solid-state samples.

Compound	Eu($^5D_0\leftarrow{}^7F_0$) [cm^{-1}]	Site	Lifetime [ms]
[Eu(**L11**)$(NO_3)_3$] (**9**)	17233	I	0.8(1)
	17251	II	1.15(5)
	17213	III	1.05(5)
[Eu(**L10**)$(NO_3)_3$]	17215	III	1.23(4)
[Eu(**L11**)$(CF_3CO_2)_3$] (**16**)	17235	A	2.5(1)
	17247	B	0.5(1)
[Eu(**L12**)$(CF_3CO_2)_3$] (**17**)	17235	A	2.50(9)
	17246	B	0.49(4)

The Eu($^5D_0\leftarrow{}^7F_0$) excitation profile of the related trifluoroacetato complex [Eu(**L12**)$(CF_3CO_2)_3]_2$ (**17**), for which a dimeric structure has been unambiguously assigned for the analogous lutetium complex **18** (Figure 1), also shows two peaks, with major site A (17 235 cm^{-1} at 10 K) and a weak shoulder assigned to site B (17 246 cm^{-1} at 10 K, Figure 4d), a situation strictly mirrored in the lipophilic complex [Eu(**L11**)$(CF_3CO_2)_3]_2$ (Figure 4c), which can be therefore assigned as a centrosymmetrical dimer in the solid state. Application of Equation (1) predicts $\bar{\nu}_{calcd}=17\,242\ cm^{-1}$ for the eight-coordinated Eu^{III} atom in [Eu(**L12**)$(CF_3CO_2)_3]_2$ at 295 K, which changes to $\bar{\nu}_{calcd}=17\,230\ cm^{-1}$ at 10 K, a prediction in fair agreement with

17235 cm^{-1} experimentally observed for the major site A (> 85%). The nature of the Eu^{III} environment in the minor site B is more difficult to address, but we notice that: 1) deviation from axial symmetry is larger in the emission spectra obtained upon selective excitation of this site (see Figures S7 and S8 in the Supporting Information) and; 2) the Eu($^5D_0$) lifetime is reduced from 2.5(1) ms in site A to 0.45–0.50 ms in site B (10 K, Table 2). Assuming $\tau_{D2O}=\tau$(Eu($^5D_0$)) for the nonhydrated Eu^{III} site A (2.50 ms, Table 2) in Equation (2), and τ(Eu($^5D_0$)) = 0.50 ms for site B (τ_{H2O} in Eq. (2)), The Horrocks–Sudnick Equation 2[28] estimates that $q^{Eu}_{H2O}=1.9\approx 2$ additional water molecules are bound to each Eu^{III} in the minor site B, a general trend for mid-range Eu^{III}, which tends to increase its coordination number from CN = 8 (in site A) to CN = 9 or 10 (in site B).

$$q^{Eu}_{H2O} = 1.05 \cdot (\tau^{-1}_{H20} - \tau^{-1}_{D20}) \quad (2)$$

In conclusion, the nitrato complex [Eu(**L11**)$(NO_3)_3$] (**9**) exists in the solid state mainly in its monomeric form, in which the central metal is nine-coordinated by the tridentate ligand **L11** and three bidentate nitrate anions. An extra water molecule can be added to form a ten-coordinate monomer depending on the experimental conditions. The formation of traces of the dimer [Eu_2(**L11**)$_2(NO_3)_6$], detected for the mid-range Eu^{III} cation, are also expected for larger Ln^{III}. On the other side, the trifluoroacetato complex [Eu(**L11**)$(CF_3CO_2)_3]_2$ (**16**) exists exclusively as a centrosymmetrical dimer in the solid state. These behaviors exactly mirror those previously reported for the analogous complexes [Eu(**L10**)$(NO_3)_3$][18] and [Eu(**L10**)$(CF_3CO_2)_3]_2$[19] with the parent hexacatenar ligand.

Characterization and properties of the ligand L11 and of its lanthanide complexes [Ln(L11)$(NO_3)_3$] (Ln = La–Lu, Y) and [Eu(L11)$(CF_3CO_2)_3]_2$ in the liquid crystalline state: For the ligand and complexes, a first heating–cooling cycle (25–150–25 °C) was performed by using differential scanning calorimetry (DSC) for removing the cocrystallized water molecules. In each case, we checked that the structures were not affected by this process by using IR, ^{1}H NMR, and elemental analyses. The original DSC traces were very similar to those observed during further heating–cooling cycles, except for additional endotherms corresponding to the loss of water molecules occurring during the first cycle. The rest of the discussion of the thermal properties refers to second or further heating–cooling cycles. The DSC trace of the dodecatenar ligand **L11** shows two successive and reversible first-order phase transitions corresponding to the melting (T_m = −34 °C, $\Delta H^{L11}_m = 54.8$ kJ mol^{-1} and $\Delta S^{L11}_m = 226$ J $mol^{-1}K^{-1}$) and the clearing (T_c = 56 °C, $\Delta H^{L11}_c = 9.7$ kJ mol^{-1} and $\Delta S^{L11}_c = 30$ J $mol^{-1}K^{-1}$) processes (Table 3, see also Figure S9 in the Supporting Information). The programmed large melting entropy, resulting from the relaxation of the organization of the twelve divergent dodecyloxy chains per ligand in the microsegregated solid was not overcome by a comparable increase in enthalpy, which resulted in a low temperature of melting $T_m = \Delta H_m/\Delta S_m$, compatible with liquid-crystalline properties at room temperature.

A viscous and noncharacteristic birefringent texture was observed by polarized light microscopy (PLM) in the −34 °C to 56 °C domain (see Figure S10a in the Supporting Information), but the detection of two diffraction peaks at d_{001} = 36.1 Å and d_{002} = 18.0 Å in the small-angle X-ray diffraction (SA-XRD) profile, together with a broad reflection at 4.5 Å, typical for the molten alkyl chains, may be tentatively assigned to the formation of a layered organization of the ligand in the liquid-crystalline state (Table 3 and Table S5 in the Supporting Information). The collapse of these reflections for $T \geq 60$ °C is diagnostic for the formation of the liquid at the clearing temperature. A rough structural model of **L11** based on the crystal structure of coordinated **L12** in **18**, to which twelve dodecyloxy chains in optimized conformations have been added (molecular mechanics optimization in the gas phase with DSViewer Pro 5.0, Accelrys) shows a global ovoidal shape of 59 × 34 × 30 Å (see Figure S11 in the Supporting Information). The two short axes are compatible with the interlayer separation observed in the mesophase (d_{001} = 36.1 Å), which would bring the long axis of the ellipse parallel to the layer plane in a SmA organization. The molecular area $A_m = V_{mol}/d_{001} = 148$ Å^2 occupied by one ligand **L11** at 35 °C can be calculated from the molecular volume $V_{mol} = (MM \times 10^{24}/N_{Av})\ (V^T_{CH2})/V^{25\circ C}_{CH2}) = 5325.7$ Å^3, whereby $MM = 3183.83$ g mol^{-1} is the molecular weight of **L11**, N_{Av} is the Avogadro number, $\rho = V^{25\circ C}_{CH2}/V^T_{CH2}$ is the density in the mesophase and $V^T_{CH2} = 26.5616 + 0.02025T$ is the volume of a methylene unit at the temperature T [°C].[29] Since there are six alkyl chains occupying the molecular area on each part of the molecule in the layered organization (Figure 5a), we eventually obtain $a_m = 148/6 = 24.7$ Å^2 as the cross-sectional area of each chain, a value in good agreement with a_m = 22–25 Å^2 expected for a SmA organization.[29] However, we cannot completely exclude an alternative hexagonal columnar arrangement Col_h for the tabular ligand **L11**, in which the two diffraction peaks detected at 36.1 and 18.0 Å would correspond to the reflection (hk) = (10) and (20) with squared spacing ratios $1/d^2_{hk} \propto h^2 + k^2 + hk = 1$ and 4, respectively, whereas the intensity of (hk) = (11) with $d^2_{10}/d^2_{11} = 3$ should be too weak to be detected. In the latter case, the intercolumnar separation is given by $a = (2/\sqrt{3})(d_{10}) = 41.7$ Å and the calculated surface of the column amounts to $S = a \cdot < d_{10} > = 1505.4$ Å^2 (Figure 5b). The periodicity in the column is then given by $h = Z\ V_{mol}/S = 3.54$ Å for one ligand per slice (Z = 1), which is compatible with intermolecular close stacking between aromatic rings.

Compared with the hexacatenar ligand **L10** ($g \xrightarrow{25\,^\circ C} Col_h \xrightarrow{61\,^\circ C} I$, $a = 41.1$ Å),[18] the perpendicular connection of six additional dodecyloxy chains in **L11** does not drastically increase the size of the cross section of the column, but it transforms a glassy melting transition into a first-order melting transition, for which ΔH_m and ΔS_m are easily obtained by DSC. The latter observation merits some comments. According to the Ehrenfest classification, a first-order phase transition is characterized by an infinite varia-

Table 3. Phase-transition temperatures, enthalpy and entropy changes and organizations in the mesophases as deduced from SA-XRD measurements for the ligand **L11** and its complexes [Ln(**L11**)$(NO_3)_3$] (Ln = La–Lu) and [Eu(**L11**)$(CF_3CO_2)_3$].

Compound	Transition[a]	T [°C]	ΔH [kJ mol^{-1}]	ΔS [J mol^{-1} K^{-1}]	SA-XRD[b]
L11	Cr→SmA or Col_h	−34	54.8	226	SmA: d_{001} = 36.1 Å, A_m = 148 Å^2
					Col_h: a = 41.7 Å, S = 1505 Å^2, h = 3.54 Å
	SmA or Col_h→I	56	9.7	30	
	I→dec	320			
[La(**L11**)$(NO_3)_3$] (**6**)	Cr→SmA or Col_h	−25	46.7	188	SmA: d_{001} = 33.7 Å, A_m = 173 Å^2
					Col_h: a = 38.9 Å, S = 1312 Å^2, h = 4.44 Å
	SmA or Col_h → Cub	110–130	–	–	Cub$I$, a = 48.78 Å V = 116 075 Å^3,
	Cub→dec	240			
[Pr(**L11**)$(NO_3)_3$] (**7**)	Cr→SmA or Col_h	−43	54.2	236	SmA: d_{001} = 33.8 Å, A_m = 172 Å^2
					Col_h: a = 39.0 Å, S = 1318 Å^2, h = 4.42 Å
	SmA or Col_h → Cub	110–130	–	–	Cub$I$, a = 50.0 Å, V = 125 000 Å^3,
	Cub→dec	207			
[Sm(**L11**)$(NO_3)_3$] (**8**)	Cr→Col_h	−34	59	247	a = 39.14 Å, S = 1328 Å^2, h = 4.68 Å, *p6mm*
	Col_h→dec	208			
[Eu(**L11**)$(NO_3)_3$] (**9**)	Cr→Col_h	−31	58.2	240	a = 38.75 Å, S = 1300 Å^2, h = 4.75 Å, *p6mm*
	Col_h→dec	220			
[Gd(**L11**)$(NO_3)_3$] (**10**)	Cr→Col_h	−32	61.6	256	[c]
	Col_h→dec	220			
[Tb(**L11**)$(NO_3)_3$] (**11**)	Cr→Col_h	−33	55.5	231	[c]
	Col_h→dec	214			
[Yb(**L11**)$(NO_3)_3$] (**13**)	Cr→Col_h	−32	58.6	246	a = 38.49 Å, S = 1283 Å^2, h = 4.84 Å, *p6mm*
	Col_h→dec	240			
[Lu(**L11**)$(NO_3)_3$] (**14**)	Cr→Col_h	−32	62.5	259	a = 39.28 Å, S = 1336 Å^2, h = 4.41 Å, *p6mm*
	Col_h→dec	231			
[Y(**L11**)$(NO_3)_3$] (**15**)	Cr→Col_{h1}	−35	39.6	166	a = 39.12 Å, S = 1325 Å^2, h = 4.16 Å, *p6mm*
	Col_{h1}→Col_{h2}	14	12.7	44	a = 39.14 Å, S = 1327 Å^2, h = 4.31 Å, *p6mm*
	Col_{h2}→SmA	91	4.8	13	d_{001} = 33.2 Å, A_m = 184 Å^2
	SmA→dec	229			
[Eu(**L11**)$(CF_3CO_2)_3$] (**16**)	Cr→Col_h	−37	67.1	284	a = 37.74 Å, S = 1233 Å^2, h = 4.90 Å, *p6mm*
	Col_h→I	139	13.6	33	
	I→dec	260			

[a] Cr: crystal, Col_h: hexagonal columnar phase, Cub: cubic columnar phase, SmA: smectic A, I: isotropic fluid, dec: decomposition. First-order transition temperatures are given as the onset of the peak observed during the second heating processes (Seiko DSC 220C differential scanning calorimeter, 5 °C min^{-1}, under N_2); the liquid crystalline phases were identified from their optical textures and from SA-XRD studies. [b] $A_m = V_{mol}/d_{001}$ is the molecular area occupied by one molecule in a smectic phase. S is the lattice area of the column $S = a < d_{10} > = a^2 \cdot \sin(60)$ and $h = ZV_{mol}/S$ the periodicity of the molecules along the column (Z = 1) in a hexagonal columnar mesophase (Col_h); V is the volume of the unit cell in the cubic mesophase ($V_{mol} = (MM \times 10^{24}/N_{AV})(V^T_{CH2}/V^{25°C}_{CH2})$ is the molecular volume, $V^T_{CH2} = 26.5616 + 0.02025T$ is the volume of a methylene unit at the temperature T (°C) and $\rho = V^{25°C}_{CH2}/V^T_{CH2}$ is the estimated density of the mesophase at the temperature, T).[29] [c] No SA-XRD data recorded for this complex.

tion of the heat capacity $C_P = \left(\frac{\partial H}{\partial T}\right)_P \rightarrow \infty$ at the temperature of melting, because the enthalpy H changes by a finite amount for an infinitesimal change of temperature.[30] Such a situation occurs when the entropy of mixing is negligible during the phase transition, a situation that occurs, for example, during the melting of ice into liquid water because the two phases cannot be homogeneously mixed. This behavior usually originates from significantly different structures and organizations in the two phases and/or from high viscosity, which severely limits dispersion of one phase into the other at the melting temperature. For a transition involving the transformation of a microsegregated solid, into a mesophase possessing similar organizations, as found in **L11**, the first-order transition can be thus reasonably ascribed to the considerable viscosity of the material at the temperature of melting (−34 °C), which hampers the intimate mixing of the phases and the operation of significant mixing entropy as a driving force. The crystallization process (−40 °C) produces SA-XRD patterns dominated by the 36.1 and 18.0 Å reflections, together with novel smaller peaks highlighting some improved organization in the solid state.

Interestingly, the complexation of **L11** to Eu^{III} in the dimeric complex [Eu(**L11**)$(CF_3CO_2)_3]_2$ (**16**) does not strongly influence the melting temperature (T_m = −37 °C). The thermodynamic parameters of the first-order phase transition (Figure 6a and Table 3) are still dominated by a massive melting entropy (ΔS_m = 284 J mol^{-1} K^{-1}), whereas we observe a considerable shift of the clearing temperature in the complex, which results from a 40 % increase of the clearing enthalpy ($\Delta T_c = T_c([Eu(\mathbf{L11})(CF_3CO_2)_3]_2) - T_c(\mathbf{L11}) = +83$ °C, Table 3). No significant decomposition was observed over several heating–cooling cycles assuming that the complex is not kept in the liquid phase for a long period (1 h). We assign the larger clearing enthalpy in the complex to the rigidification of the aromatic core consecutive to the complexation of the metal, which improves intermolecular cohesion within the residual organized clusters in the mesophase. PLM observations display a noncharacteristic and poorly developed birefringent texture in the −30 to 130 °C domain (see Figure S10b in the Supporting Information), but SA-XRD patterns unambiguously show up to seven reflections with squared spacing ratios $1/d^2_{hk} \propto h^2 + k^2 + hk$ = 1, 3, 4, 7, 9,

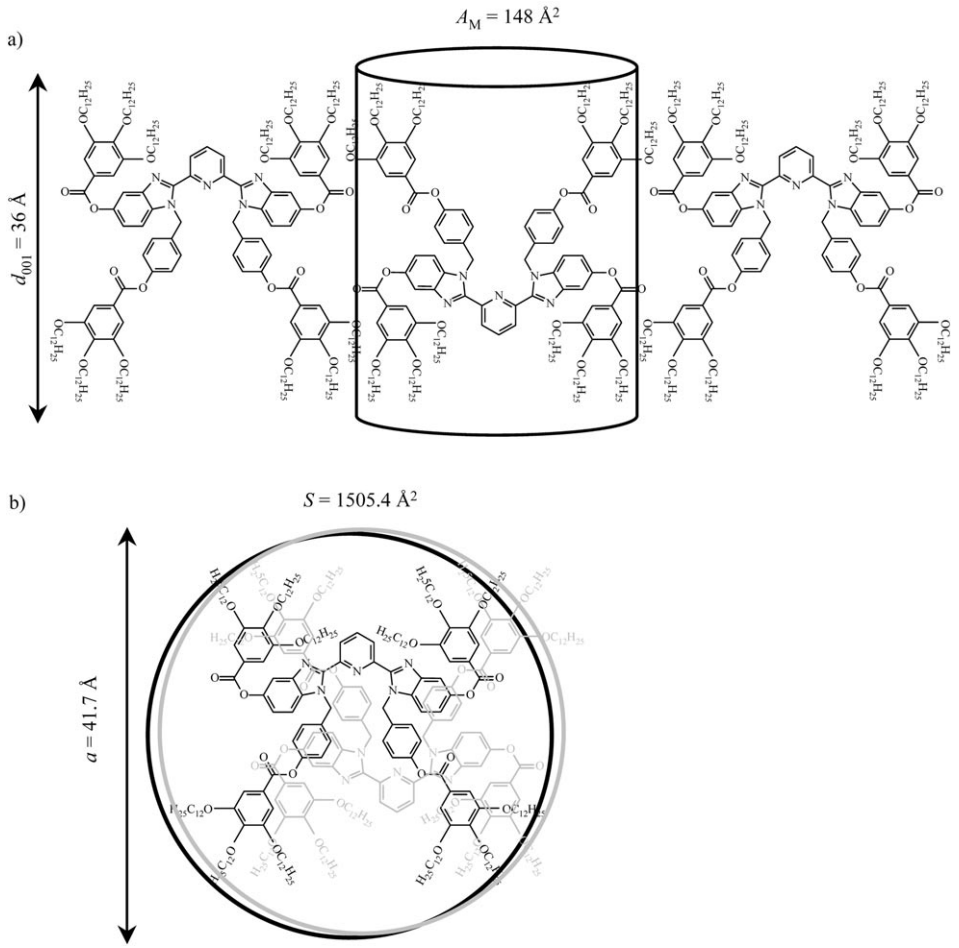

Figure 5. Schematic organization proposed for the ligand **L11** in a) SmA and b) Col_h mesophases.

12, 13 ((*hk*) = (10), (11), (20), (21), (30), (22), (31), respectively) supporting the formation of a well-correlated hexagonal columnar arrangement (Figure 7, Col_h, plane group *p*6 or *p6mm*, Table 3, see also Table S5 in the Supporting information).[29] The mathematical analysis leads to an intercolumnar separation $a = 37.7$ Å associated with a cross-sectional area of the rigid core amounting to $S = (\sqrt{3}/2)\cdot a^2 = 1233$ Å^2 (Table S5 in the Supporting Information). The detection of a weak, but reproducible reflection at 5.83 Å, reminiscent of the Lu···Lu distance found in the crystal structure of [Lu(**L12**)$(CF_3CO_2)_3]_2$ (**18**, Lu···Lu = 5.44 Å), indicates the conservation of the bridged dimeric structure in the mesophase. Taking a reasonable density of $\rho = 1.0$ g cm^{-3} at 25 °C in the hexagonal columnar mesophase,[29] we calculate a molecular volume $V_{mol} = 6041.5$ Å^3 for the asymmetric monomeric unit, and thus a periodicity of $h = Z\ V_{mol}/S = 4.90$ Å for a mononuclear disk-like unit along the column. The 40 % increase in thickness per ligand unit in going from **L11** ($h = 3.54$ Å) to [Eu(**L11**)$(CF_3CO_2)_3$] ($h = 4.90$ Å) reflects the extension of the bulky aromatic rigid core upon coordination of $Eu(CF_3CO_2)_3$. Compared with the 27 Å diameter estimated for the rigid core of the complex [Lu(**L12**)$(CF_3CO_2)_3]_2$ (**18**, Figure 2), the only 10 Å larger diameter found for the column in the mesophase of [Eu(**L11**)$(CF_3CO_2)_3]_2$ (37.7 Å) implies interdigitation between the molten dodecyloxy chains, because a single twelve-carbon unit chain in all-*trans* conformation extends to approximately 15 Å.

A very similar behavior is observed for the heavy and mid-range lanthanides in the nitrato complexes [Ln(**L11**)$(NO_3)_3$] (Ln = Sm–Lu, Table 4, and Table S4, and Figure S10c in the Supporting Information), which display entropically-driven ($236 \le \Delta S_m \le 259$ J mol^{-1} K^{-1}, Table 3) low-temperature first-order melting processes ($-37 \le T_m \le -30$ °C, Figure 6b), leading to columnar hexagonal organizations in the mesophase ($38 \le a \le 39$ Å, Table S5 in the Supporting Information). In contrast with the trifluoroacetate parent complex **16**, the nitrato complexes show much higher clearing temperatures ($214 \le T_c \le 240$ °C), followed by decomposition in the liquid. However, DSC traces show the melting processes to be fully reversible provided the clearing temperature is not reached during the heating–cooling cycle. It is worth noting that, in contrast to [Eu(**L11**)$(CF_3CO_2)_3]_2$, no specific diffraction peak corresponding to bridged Ln pairs can be detected by SA-XRD in the hexagonal columnar mesophases of the nitrato complexes [Ln(**L11**)$(NO_3)_3$] (Ln = Sm–Lu), in agreement with the limited affinity of NO_3^- to act as rigid bridges between two trivalent lanthanides.

For the complexes with the larger lanthanides (La, Pr), the first-order melting transition still occurs at low temperature (Table 3), but the single diffraction peak in the SA-XRD patterns, combined with the observation of birefringent textures by PLM, are compatible either with lamellar phases at room temperature ($d_{001} = 33.5$–33.7 Å, $A_m = 166$–173 Å^2, $a_m = A_m/6 = 27.7$–28.8 Å^2, Table 4 and Table S4 in the Supporting Information), or with hexagonal columnar mesophases ($d_{10} = 33.5$–33.7 Å, $a = 38.7$–38.9 Å, $S = 1300$–1312 Å^2, $h = 4.30$–4.44 Å, Table 4 and Table S4 in the Supporting Information) as previously discussed for the free ligand (Figure 5). The calculated cross section of each alkyl chain ($a_m = 27.7$–28.8 Å^2) exceeds that expected for standard SmA organizations ($a_m = 22$–25 Å^2), which suggests that the alternative assignment to standard Col_h organizations is more ap-

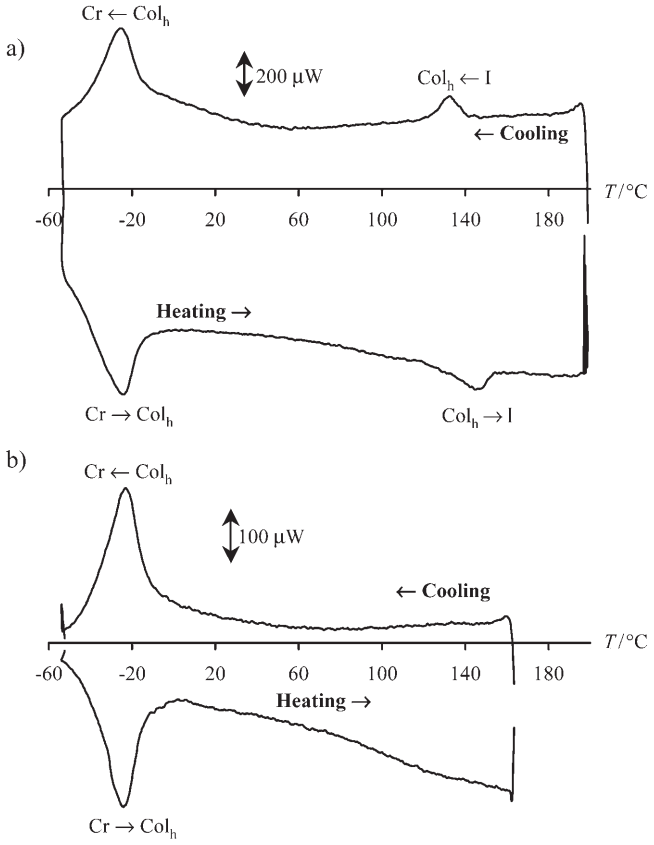

Figure 6. DSC traces of a) [Eu(**L11**)$(CF_3CO_2)_3$] (**16**) and b) [Eu(**L11**)-$(NO_3)_3$] (**9**) (5 °C min^{-1} under N_2, 1st cooling process, 2nd heating process).

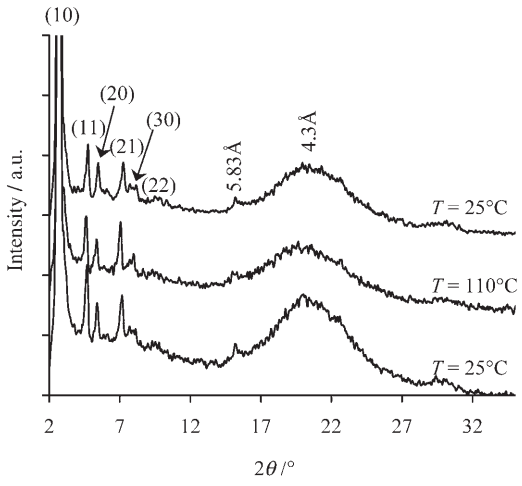

Figure 7. SA-XRD profiles in the liquid crystalline phase, and associated indexation for [Eu(**L11**)$(CF_3CO_2)_3$] (**16**) obtained upon a heating–cooling cycle.

propriate (tilted SmC organizations cannot be ruled out, but they are unlikely because of the observation of homeotropic zones in the birefringent textures). These latter phases slowly tend to form cubic phases around $T = 110$–160 °C (no

Table 4. Formation constants of [Ln(**L10**)$(NO_3)_3$] ($\log(\beta_{1,1}^{Ln,L10})$[18] and of [Ln(**L11**)$(NO_3)_3$] ($\log(\beta_{1,1}^{Ln,L11})$ at 293 K.

Complexes	$\log(\beta_{1,1}^{Ln,L10})$[a] CH_2Cl_2/CH_3CN (1:1)	$\log(\beta_{1,1}^{Ln,L11})$[a] CH_2Cl_2/CH_3CN (1:1)	$\log(\beta_{1,1}^{Ln,L11})$[b] $CDCl_3$
[La(**L*i***$)(NO_3)_3$]	5.7(2)	4.5(1)	<0.7
[Pr(**L*i***$)(NO_3)_3$]	–	4.9(1)	1.5(1)
[Eu(**L*i***$)(NO_3)_3$]	5.3(2)	5.0(2)	2.1(1)
[Tb(**L*i***$)(NO_3)_3$]	–	4.6(1)	
[Ho(**L*i***$)(NO_3)_3$]	–	4.8(1)	
[Yb(**L*i***$)(NO_3)_3$]	–	5.3(1)	3.3(1)
[Lu(**L*i***$)(NO_3)_3$]	6.1(1)	5.5(2)	>4.5
[Y(**L*i***$)(NO_3)_3$]	5.9(1)	4.9(2)	3.0(1)

[a] Determined by spectophotometric titrations. [b] Determined by ^{1}H NMR titrations.

birefringent texture by PLM accompanied by orthorhombic flashes obtained upon applying specific pressure on the preparation) characterized by squared spacing ratios $1/d_{hk}^2 \propto h^2+k^2+l^2 = 2$, 4, 8 for body-centered Cub*I* organizations (Table 4 and Table S4 in the Supporting Information). This broad antiLandau[31] lamellar or columnar→cubic phase transition has been previously reported and discussed for the analogous complexes [Ln(**L10**)$(NO_3)_3$] (Ln: La–Nd) with the hexacatenar parent ligand. It was eventually assigned to the stepwise thermally-driven entropic dissociation of initial dimeric complexes [Ln_2(**L*i***$)_2(NO_3)_6$] existing at low temperature for the large lanthanides, into monomers [Ln(**L*i***$)(NO_3)_3$] ($i = 10$, 11) at high temperature in the mesophase.[18] The intensity of the reflections detected in the cubic mesophases are weak (two reflections for [La(**L11**)-$(NO_3)_3$] and three for [Pr(**L11**)$(NO_3)_3$], see Table S5 in the Supporting Information), and we were unable to observe the intermediate (211) reflection, which precludes more accurate interpretation of the SA-XRD data for these complexes. However, in analogy with the unambigous assignment of $Im\bar{3}m$ space group for strictly analogous behaviors reported for [Ln(**L10**)$(NO_3)_3$] (Ln = La–Nd),[18] we tentatively attribute the same space group for the extended complexes [Ln(**L11**)$(NO_3)_3$] (Ln = La, Pr) in their cubic phase. It is worth noting that the nonlanthanide complex [Y(**L11**)-$(NO_3)_3$] (**15**) displays a specific thermal behavior, although it is well established that its coordination properties are very similar to Ho^{III}, a heavy lanthanide of similar size. For [Y-(**L11**)$(NO_3)_3$], the first-order melting process Cr→Col$_h$ occurs in two steps, the combined enthalpies and entropies of which compare well with those found for the unique melting process recorded for the complexes [Ln(**L11**)-$(NO_3)_3$] with the heavy lanthanides Ln: Eu–Lu (Table 3, and Figure S12 in the Supporting Information). The organization in the Col$_h$ mesophase is similar to that observed for lanthanide complexes of similar sizes (Table 3), but a second reversible first-order Col$_h$→SmA ($d_{001} = 33.2$ Å, Table 3), reminiscent of that found for the free ligand at lower temperature, occurs at 91 °C, prior to isotropization ($T_c = 229$ °C). We suspect that the change in polarizability in going from trivalent lanthanides ([Xe]4f^n) to trivalent yttrium ([Kr]) affects some

intermolecular interactions involving the rigid core, thus leading to different organization of the residual clusters in the mesophases. This phenomenon is reminiscent of the drastic decrease in hyperpolarizability observed when Y^{III} replaces Ln^{III} in the closely related nonlinear optically active complexes [Ln(2,2′:6′,2″-terpyridine)$(NO_3)_3$], a behavior similarly ascribed to the reduced number of electrons in the metal.[32] Finally, the SA-XRD profiles recorded at −40 °C for all complexes show that the first-order crystallisation process leads to a poorly organized solid in which the prior columnar organizations dominate the diffractograms.

To further explore the nature and magnitude of the structural changes accompanying these first-order melting transitions, we have turned to temperature-dependent high-resolution emission spectra recorded for the complex [Eu(**L11**)-$(NO_3)_3$] (**9**), in which Eu^{III} acts as a luminescent probe.[18,33] A thin film of [Eu(**L11**)$(NO_3)_3$], deposited and dried (150 °C for a short period) on a quartz surface, shows a broad Eu-($^5D_0 \leftarrow {}^7F_0$) excitation profile at 10 K (17235 cm^{-1}, full-width-at-half-height, fwhh = 30 cm^{-1}) covering the same spectral domain as that found for the bulk solid in **9**, which is typical for a polycrystalline material containing a large number of Eu^{III} sites with very similar environments (see Figure S13 in the Supporting Information).

The emission spectra recorded below (−50 °C) and above (0 °C) the melting temperature do not show significant variations in the crystal-field splitting (Figure 8a), in agreement with SA-XRD diffractograms, thus pointing to a minor structural change accompanying the first-order phase transition. However, the variation in intensity of the total luminescence originating from the Eu($^5D_0$) excited level indeed produces a sigmoid curve for plots of $\ln(I_{obs}/I_{263K})$ versus the inverse of the temperature (T^{-1}, Figure 8c) with a convex-to-concave transition occurring at −41 °C (see Figure S14 in the Supporting Information), in going through the first-order melting transition (Figure 8b). Since a linear dependence $\ln(I_{obs}/I_{263K}) = -C/RT$ is theoretically predicted (C is a constant and R is the molar gas constant),[34] and experimentally observed when no first-order phase transition occurs,[18,33] we conclude that luminescence is extremely sensitive to minor changes around Eu^{III} occurring during the melting process.

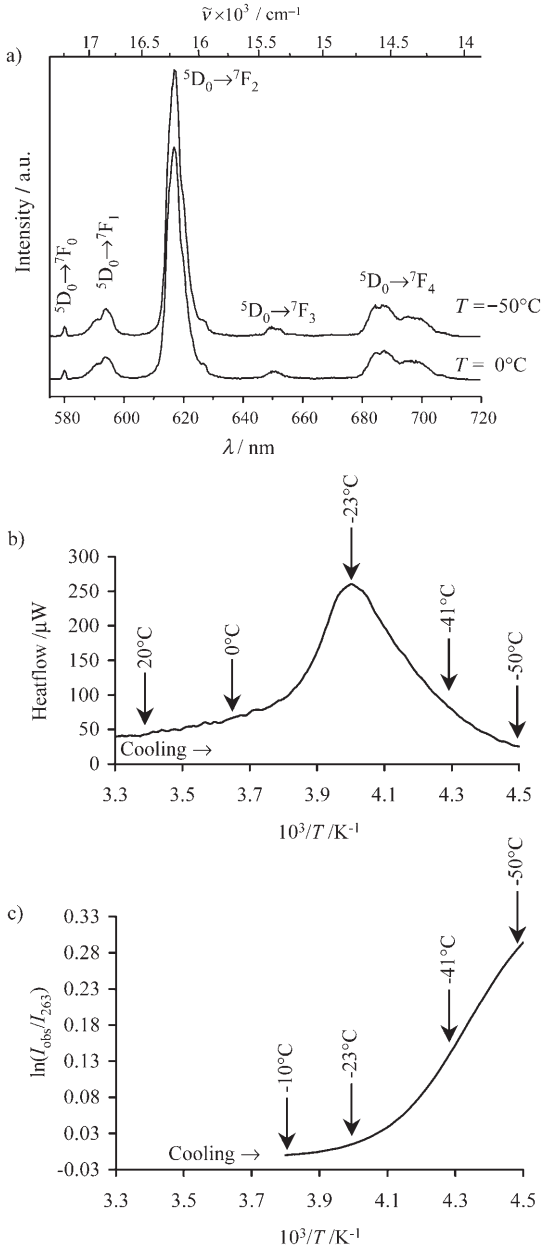

Figure 8. a) Steady-state high-resolution emission spectra of a film of [Eu(**L11**)$(NO_3)_3$] at 273 K and 223 K, b) DSC trace and, c) plot of $\ln(I_{obs}/I_{263K})$ versus the inverse of the absolute temperature for the crystallization of a film of [Eu(**L11**)$(NO_3)_3$] ($\bar{\nu}_{exc}$ = 28410 cm^{-1}).

Characterization and properties of the ligand L11 and of its lanthanide complexes [Ln(L11)$(NO_3)_3$] (Ln = La–Lu, Y) in isotropic solutions: Although the structure and properties of the lipophilic nitrato complexes [Ln(**L11**)$(NO_3)_3$] in the liquid state at high temperature cannot be determined because of fast oxidative decomposition,[15–18] their thermodynamic and structural behaviors can be obtained by investigating their solution properties in nonpolar, or weakly polar solvents. Spectrophotometric titrations of **L11** (10^{-4} M) with $Ln(NO_3)_3 \cdot x H_2O$ (x = 2–4, Ln = La, Pr, Eu, Tb, Ho, Yb, Lu, Y) in CH_2Cl_2/CH_3CN (1:1) show the expected red-shift of the ligand-centered $\pi \rightarrow \pi^*$ transitions occurring upon complexation (Figure 9a). A single end point for a ratio Ln:**L11** = 1.0 is systematically detected (Figure 9b), and the spectrophotometric data can be satisfyingly fitted to equilibrium (3) by using nonlinear least-squares techniques.[35]

$$\mathbf{L11} + Ln(NO_3)_3 \rightleftharpoons [Ln(\mathbf{L11})(NO_3)_3] \quad \beta_{1,1}^{Ln,L11} \qquad (3)$$

The formation constants $\beta_{1,1}^{Ln,L11}$ obtained with the dodecatenar ligand **L11** and collected in Table 4 are smaller by one order of magnitude than those found with the hexacatenar ligand **L10** in the same conditions.[18] This detrimental feature can be traced back to the connection of bulky benzyl substituents to the noncoordinating nitrogen atoms of the

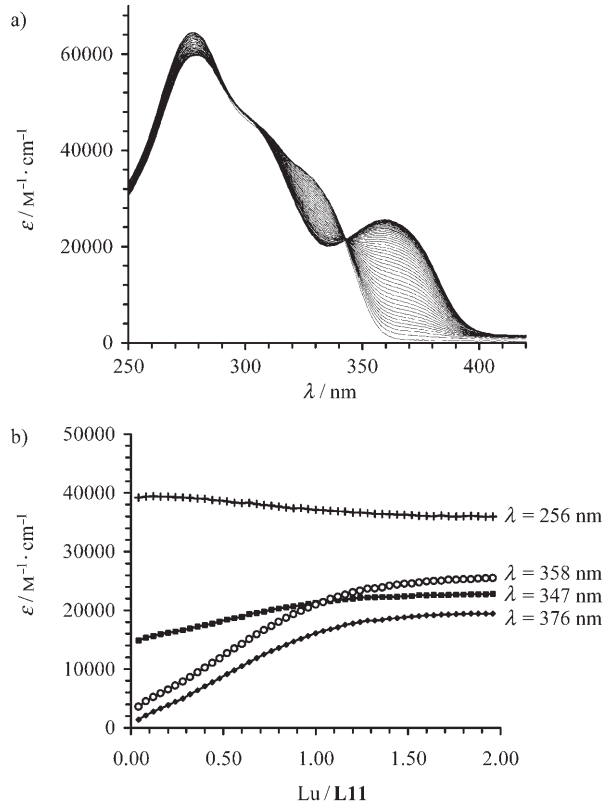

Figure 9. a) Variation of absorption spectra observed for the spectrophotometric titration of **L11** (10^{-4} M in acetonitrile/dichloromethane (1:1)) with $Lu(NO_3)_3{\cdot}3H_2O$ at 293 K (Lu: **L11** = 0.05–2.0). b) Corresponding variation of observed molar extinctions at four different wavelengths.

benzimidazole rings in **L11**, which produces strong steric constraints with the *meta* protons of the central pyridine (H2 in Figure 10) during the *trans–trans*→*cis–cis* conformational change required for the complexation of the metal, a phenomenon previously documented for the bulky ligand 2,6-bis(1-(3,5-dimethoxybenzyl)benzimidazol-2-yl)pyridine.[22,36] These rather small stability constants $\beta_{1,1}^{Ln,L11}$ are poorly sensitive to the lanthanide size, but estimating the quantum yield in solution for $|[Ln(\mathbf{L11})(NO_3)_3]|_{tot} = 3 \times 10^{-5}$ M (Ln = Eu, Tb) requires calculation of the effective absorption of the complex because only 43 % of the ligand is coordinated to Ln^{III} at this concentration. Taking $Cs_3[Ln(dipicolinate)_3]$ in aqueous solution as external reference (Ln = Eu, Tb)[37] and neglecting the faint emission arising from directly excited noncomplexed $Eu(NO_3)_3$, we obtain absolute quantum yields $\Phi_{abs}([Eu(\mathbf{L11})(NO_3)_3]) = 0.28(5)$ and $\Phi_{abs}([Tb(\mathbf{L11})(NO_3)_3]) = 0.06(2)$ in dichloromethane:acetonitrile at 295 K ($\bar{\nu}_{exc} = 35\,840\ cm^{-1}$). The latter small value exactly matches that reported for [Tb(**L10**)$(NO_3)_3$] and originates from the efficient thermally-activated $Tb(^5D_4) \rightarrow \mathbf{Li}(^3\pi\pi^*)$ ($i = 10$, 11) back transfer operating between these two almost resonant levels.[24] The case of Eu^{III} is remarkable because both light-harvesting (measured by $\varepsilon_{\lambda max}$) and the light-conversion (measured by Φ_{abs}) processes are improved in going from [Eu(**L10**)$(NO_3)_3$] ($\varepsilon_{285nm} = 41\,000\ M^{-1}\ cm^{-1}$; $\Phi_{abs} = 6\,\%$)[14] to [Eu(**L11**)$(NO_3)_3$] ($\varepsilon_{285nm} = 64\,000\ M^{-1}\ cm^{-1}$; $\Phi_{abs} = 28\,\%$). Since the $Eu(^5D_0)$ lifetimes display the opposite trend with $\tau = 1.23$ ms for [Eu(**L10**)$(NO_3)_3$] and $\tau = 1.05$ ms for [Eu(**L11**)$(NO_3)_3$] (Table 2), we conclude that the improved quantum yield results from a more efficient **L11**→Eu^{III} energy-funneling process. The eventual origin of this phenomenon is difficult to unambiguously address, but we note that the energy of the triplet state in [Gd(**L11**)$(NO_3)_3$] ($E(^3\pi\pi^*) = 20\,325\ cm^{-1}$, Table 1) is $800\ cm^{-1}$ lower in energy than that found in [Gd(**L10**)$(NO_3)_3$] ($E(^3\pi\pi^*) = 21\,100\ cm^{-1}$),[14] a characteristic which is known to improve: 1) intersystem crossing (ISC) thanks to the increase in the ligand-centered singlet–triplet energy gap,[38] and; 2) $^3\pi\pi^* \rightarrow Eu(^5D_J,\ J = 1,\ 2)$ energy transfer processes thanks to the energy matching of the donor and acceptor levels.[39]

Finally, the ^1H NMR spectra of the complexes [Ln(**L11**)$(NO_3)_3$] (10^{-2} M in $CDCl_3$ because of precipitation in CD_2Cl_2:CD_3CN (1:1) at concentrations larger than 0.2 mM) show the expected meridional tricoordination of the ligand about the metal, which induces: 1) a significant upfield shift for the pyridine protons H2 in the diamagnetic complex [Lu(**L11**)$(NO_3)_3$] ($\Delta\delta = 0.54$ ppm, Figure 10a) and; 2) nuclear Overhauser Enhancement effect between H2–H10 (numbering in Figure 10).[18] Surprisingly, $\beta_{1,1}^{Ln,L11}$ data reported in Table 4 predict negligible decomplexation at 10 mM concentration, but the ^1H NMR spectra of lanthanides larger than Lu^{III} (Ln = La–Yb) display an increasing amount of free ligand in slow exchange with the complex (equilibrium (3), free ligand/complexed ligand $\leq 5\,\%$ for Ln: Lu and $\geq 95\,\%$ for Ln = La, Figure 10b,c and Table S6 in the Supporting Information). Integration of the ^1H NMR signals for free and bound ligands allows the straightforward estimation of $\beta_{1,1}^{Ln,L11}$, which are reduced by 2–4 orders of magnitude in $CDCl_3$ (Table 4). This spectacular change of $\beta_{1,1}^{Ln,L11}$ with solvent polarity illustrates the importance of solvation effect in lipophilic coordination complexes, and more specifically the strong contribution of the solvation of the organic part, that is, the ligand, with respect to the polar Ln$(NO_3)_3$ core.

Conclusion

In line with previous work in this field,[18,19,22,36] the connection of bulky lipophilic benzyl residues to the noncoordinating nitrogen atom of the benzimidazole rings in **L11** is harmful for the stability of the resulting [Ln(**L11**)$(NO_3)_3$] and [Ln(**L11**)$(CF_3CO_2)_3$] complexes, but the formation constants measured in isotropic solutions are large enough to ensure the conservation of the integrity of the complexes in solid, liquid-crystalline, and liquid states. The connection of six additional divergent dodecyloxy chains in going from **L10** to the novel dodecacatenar ligand **L11**, produces huge programmed melting entropies ($180 \leq \Delta S_m \leq 280\ J\,mol^{-1}\,K^{-1}$), which are only partially balanced by enthalpic gains, and which results in unprecedented low-temperature melting processes for the lanthanidomesogens [Ln(**L11**)$(NO_3)_3$] and

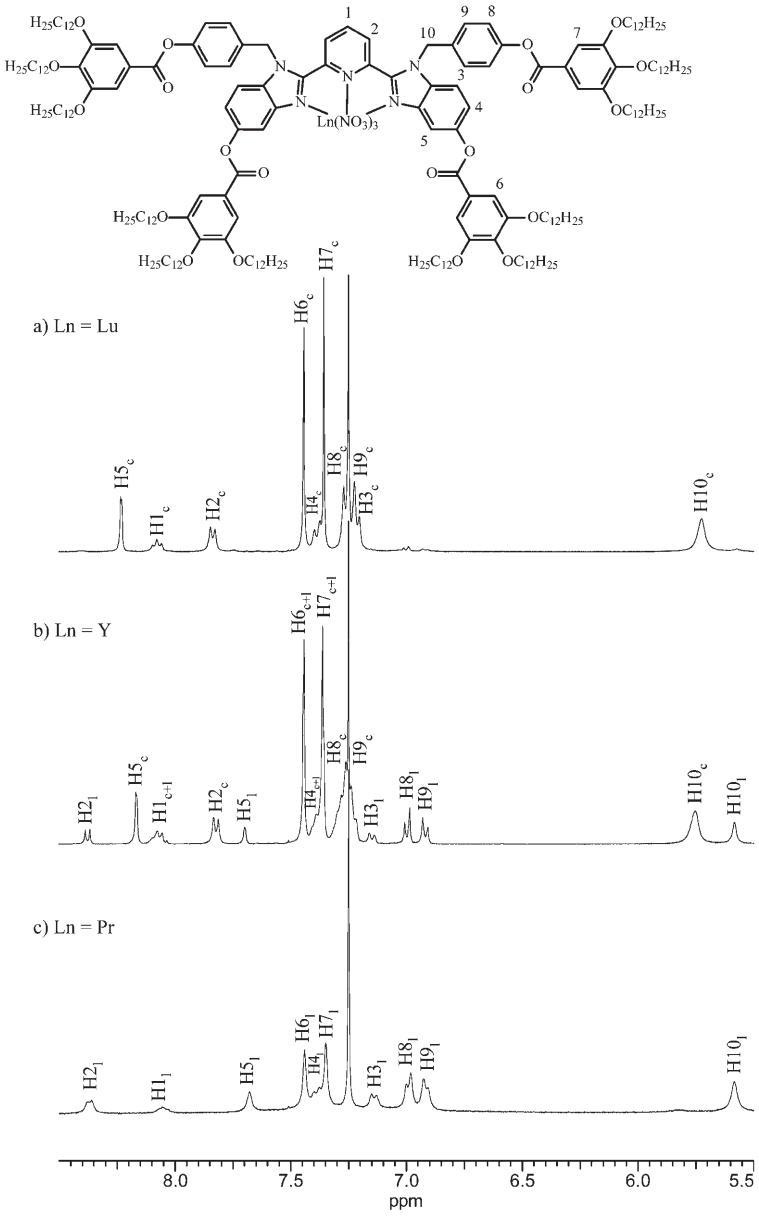

Figure 10. ^{1}H NMR spectra with numbering scheme for a) [Lu(**L11**)$(NO_3)_3$] (<5% decomplexation), b) [Y(**L11**)$(NO_3)_3$] (26% decomplexation), and c) [Pr(**L11**)$(NO_3)_3$] (81% decomplexation). The indices c and l refer to the complex and to the free ligand, respectively.

[Ln(**L11**)$(CF_3CO_2)_3$]. The large entropically-driven decrease of the melting temperature in the latter dodecacatenar complexes (ΔT_m = 120–140 °C) has two major consequences, which are exploited in this work.

1) Lamellar and/or hexagonal columnar mesophases are produced at room temperature, which avoids thermally driven entropic decomplexation, and which ensures the conservation of intact molecular complexes in the mesophases; a prerequisite for a (supra)molecular bottom-up programming of metallomesogens.
2) The considerable viscosity of both solid- and liquid-crystalline phases at low temperature prevents an intimate mixing of the two phases during the melting process, which severely limits the contribution of the mixing entropy as a driving force for the phase transition. First-order processes thus result, which greatly facilitate the quantitative determination of enthalpic (ΔH_m) and entropic (ΔS_m) contributions. The latter parameters reported in this work systematically support our simple thermodynamic model based on the explicit consideration of two successive phase transitions, respectively mainly affecting: a) the intermolecular cohesion between the flexible part (melting) and; b) the rigid cores of the molecules (clearing).[10]

We therefore conclude that, after ΔH_c which can be rationally influenced by a judicious choice of rigid aromatic cores possessing specific alternating polarization,[14] ΔS_m is a second thermodynamic parameter which can be controlled by chemical synthesis for designing molecular objects with accessible mesomorphic properties. We do believe that the enthalpically unbalanced increase of ΔS_m in divergent polycatenar systems is a general phenomenon, which is not limited to lanthanidomesogens, but also applies to the general preparation of room-temperature metallomesogens, in which specific magnetic, electronic, or photophysical properties can be introduced. The next challenge in this field concerns the combination of both chemically-tuneable thermodynamic parameters (ΔS_m and ΔH_c) for designing complexes displaying fluid nematic phases with potential technological applications at room temperature.

Experimental Section

Chemicals were purchased from Fluka AG and Aldrich, and were used without further purification unless otherwise stated. The nitrate salts Ln-

$(NO_3)_3{\cdot}x\,H_2O$ (Ln: La–Lu, Y, $x=1$–4)[40] and $Eu(CF_3CO_2)_3{\cdot}3\,H_2O$[41] were prepared from the corresponding oxides (Aldrich, 99.99%). The Ln content of solid salts was determined by complexometric titrations with Titriplex III (Merck) in the presence of urotropine and xylene orange.[42] Acetonitrile and dichloromethane were distilled over calcium hydride. Thin-layer chromatography (TLC) was performed by using silica gel plates Merck 60 F_{254}, and Fluka silica gel 60 (0.04–0.063 mm) was used for preparative column chromatography.

Preparation of *N*-(4-methoxybenzyl)-*N*′-(2-nitro-4-methoxyphenyl)amine (2): 4-Methoxybenzyl alcohol (**1**, 20 g, 145 mmol) was stirred at room temperature with 48% aq bromhydric acid (20 mL, 175 mmol) for 45 min. The resulting solution was extracted with diethylether (3× 300 mL). The separated organic phase was washed with saturated aq $NaHCO_3$, dried with $CaCl_2$ and evaporated to dryness to give 1-bromethyl-4-methoxybenzene as a crude liquid, which was slowly added to a solution of 2-nitro-*p*-anisidine (6 g, 35,7 mmol) and *N*-ethyl-*N*-isopropylamine (12.2 mL, 71.3 mmol) in dichloromethane (50 mL) up to the disappearance of 2-nitro-*p*-anisidine (TLC: CH_2Cl_2). After washing with half-sat aq NH_4Cl (100 mL), the organic layer was separated and the aq layer was extracted with CH_2Cl_2 (3×100 mL). The combined organic phases were dried (Na_2SO_4), filtered, and evaporated to dryness. The resulting red solid was recrystallized from dichloromethane/hexane to give *N*-(4-methoxybenzyl)-*N*′-(2-nitro-4-methoxyphenyl)amine (**2**, 7.98 g, 113 mmol, yield 78%) as a red microcrystalline powder. M.p. 126–127 °C; ^{1}H NMR ($CDCl_3$): $\delta=3.75$ (s, 3H), 3.77 (s, 3H), 4.43 (s, 2H), 6.78 (d, $^3J=9.3$ Hz, 1H), 6.85 (d, $^3J=8.4$ Hz, 2H), 7.06 (dd, $^3J=9.3$ Hz, $^4J=3$ Hz, 1H), 7.24 (d, $^3J=8.4$ Hz, 2H), 7.60 ppm (d, $^4J=3$ Hz, 1H); ^{13}C NMR ($CDCl_3$): $\delta=$ 55.5, 56.1 (primary C), 47.0 (secondary), 107.3, 114.5, 115.9, 127.4, 128.5 (tertiary C), 129.7, 131.4, 141.3, 150.0, 159.3 ppm (quaternary C); MS (EI): m/z: 288.0 [M^+].

Preparation of pyridine-2,6-dicarboxylic acid bis-[*N*-(4-methoxybenzyl)-*N*′-(2-nitro-4-methoxyphenyl)amide] (3): Pyridine-2,6-dicarboxylic acid (0.73 g, 4.34 mmol) and DMF (7 μL) were refluxed in freshly distilled thionyl chloride (4.8 mL, 65.1 mmol) for 45 min. Excess thionyl chloride was distilled from the reaction mixture to give a white solid. *N*-(4-methoxybenzyl)-*N*′-(2-nitro-4-methoxyphenyl)amine (**2**, 2.5 g, 8.68 mmol) and diisopropylamine (9 mL, 52.6 mmol) were stirred in dry dichloromethane (22 mL) and the solid 2,6-dichloro-carboxypyridine previously prepared was added in one batch. The resulting mixture was refluxed for 24 h under an inert atmosphere, evaporated to dryness, partitioned between dichloromethane (50 mL) and half-sat aq NH_4Cl (100 mL). The aq layer was extracted with dichloromethane (3×100 mL), and the dried (Na_2SO_4) combined organic fractions were evaporated to dryness. The crude product was purified by column chromatography (silica gel; CH_2Cl_2/MeOH 100:0→99:1) to give 2.17 g (3.08 mmol, yield 71%) of **3** as pale-orange microcrystals. M.p. 84–86 °C; ^{1}H NMR ($CDCl_3$): $\delta=3.54$, 3.63, 3.67, 3.69, 3.78 (s, 12H), 4.24, 4.30, 4.10, 4.67, 5.25, 5.38 (d, $^3J=$ 14.4 Hz, 4H), 6.55, 6.70 (d, $^3J=8.7$ Hz, 2H), 6.81, 6.84 (d, $^3J=8.4$ Hz, 4H), 7.0 (dd, $^3J=8.7$ Hz, $^4J=3$ Hz, 2H), 7.06, 7.07 (d, $^3J=8.4$ Hz, 4H), 7.15, 7.27, 7.36 (2H, d, $^3J=8.4$ Hz), 7.31, 7.41, 7.48 (2H, d, $^4J=3$ Hz), 7.70 (m, 2H), 7.86 (d, $^3J=8.7$ Hz, 0.5H), 7.96 ppm (t, $^3J=8.7$ Hz, 0.5H); ^{13}C NMR ($CDCl_3$): $\delta=55.7$, 56.8 (primary C), 52.4, 52.6 (secondary C), 109.8, 110.6, 110.8, 114.3, 114.4, 114.7, 115.2, 120.0, 120.4, 120.5, 130.0, 130.6, 131.0, 131.1, 132.5, 133.7, 134.2 (tertiary C), 124.0, 124.8, 126.4, 127.6, 127.8, 127.5, 128.6, 128.8, 138.5, 138.6, 139.1, 139.6, 146.7, 147.0, 147.5, 151.7, 152.4, 152.7, 153.0, 159.0, 159.2, 159.4, 166.9, 167.2, 167.7, 192.0 ppm (quaternary C); MS (ES) (CH_2Cl_2): m/z: 730.2 ([M^++Na]), 708.5 ([M^++H]).

Preparation of 2,6-bis-(5-methoxy-1-(4-methoxybenzyl))-1*H*-benzimidazol-2-yl)pyridine (4): Pyridine-2,6-dicarboxylic acid bis-[*N*-(4-methoxybenzyl)-*N*′-(2-nitro-4-methoxyphenyl)amide] (**3**, 2.12 g, 3.0 mmol) was dissolved in ethanol/water (200/61 mL). Activated iron powder (2.7 g, 48.3 mmol) and concentrated hydrochloric acid (37%, 7.5 mL, 89.4 mmol) were added and the mixture refluxed for 18 h. The excess iron was separated by filtration and ethanol distilled under vacuum. The resulting mixture was poured into CH_2Cl_2 (48 mL). $Na_2H_2EDTA{\cdot}2\,H_2O$ (32.7 g, 87.8 mmol) dissolved in water (160 mL) was added and the stirred mixture was neutralized (pH 8.5) with 24% aq NH_4OH. Concentrated hydrogen peroxide (30%, 1.75 mL) was added under vigorous stirring. After 15 min, the organic layer was separated and the aq phase extracted with CH_2Cl_2 (100 mL). The combined organic phases were washed with water (3×50 mL), dried (Na_2SO_4), evaporated to dryness, and the crude residue purified by column chromatography (silica gel; CH_2Cl_2/MeOH 99:1→98:2) to give 1.46 g (2.4 mmol, yield 80%) of **4** as a white microcrystalline powder. M.p. 187–188 °C; ^{1}H NMR ($CDCl_3$): $\delta=$ 3.68 (s, 6H), 3.83 (s, 6H), 5.51 (s, 4H), 6.64 (d, $^3J=8.7$ Hz, 4H), 6.74 (d, $^3J=8.7$ Hz, 4H), 6.86 (dd, $^3J=9$ Hz, $^4J=1.8$ Hz, 2H), 7.05 (d, $^3J=9$ Hz, 2H), 7.27 (d, $^4J=1.8$ Hz, 2H), 7.83 (t, $^3J=7.8$ Hz, 2H), 7.96 ppm (t, $^3J=$ 7.8 Hz, 1H); ^{13}C NMR ($CDCl_3$): $\delta=55.4$, 56.0 (primary C), 47.9 (secondary C), 101.9, 111.6, 114.2, 114.5, 125.6, 127.8, 138.3 (tertiary C), 129.2, 131.3, 143.7, 150.0, 150.2, 156.9, 159.0 ppm (quaternary C); MS (ES) (CH_2Cl_2): m/z: 612.4 ([M^++H]).

Preparation of 2,6-bis-(5-hydroxy-1-(4-hydroxybenzyl)-1*H*-benzimidazol-2-yl)pyridine (5): 2,6-Bis-(5-methoxy-1-(4-methoxybenzyl))-1H-benzimidazol-2-yl)pyridine (**4**, 0.81 g, 1.32 mmol) was dissolved in dichloromethane (17 mL) and boron tribromide (1 M in CH_2Cl_2, 23.4 mL, 23.4 mmol) was added through a syringe under an inert atmosphere. After 21 h. stirring at RT, methanol (20 mL) was added and the resulting solution evaporated to dryness. The solid residue was suspended in water (40 mL) and the pH was set to 13–14 with NaOH (5 M). The aq phase was extracted with dichloromethane (4×50 mL), and then partially neutralized (pH 10) with concentrated hydrochloric acid. The precipitate was filtered, dried under vacuum and recrystallized from CH_2Cl_2/MeOH (1:1) to give 0.62 g (1.11 mmol, yield 84%) of **5** as beige microcrystals. M.p. >250 °C; ^{1}H NMR ([D_6]DMSO): $\delta=5.63$ (s, 4H), 6.50 (d, $^3J=8.7$ Hz, 4H), 6.71 (d, $^3J=8.7$ Hz, 4H), 6.80 (dd, $^3J=8.7$ Hz, $^4J=1.8$ Hz, 2H), 7.04 (d, $^4J=$ 1.8 Hz, 2H), 7.32 (d, $^3J=8.7$ Hz, 2H), 8.20 (t, $^3J=8.4$ Hz, 1H), 8.31 (t, $^3J=8.4$ Hz, 2H), 9.34, 9.44 ppm (s_{large}, 4H); ^{13}C NMR ([D_6]DMSO): $\delta=$ 48.0, 70.4 (secondary C), 102.9, 113.2, 115.4, 116.0, 126.8, 128.5, 139.7 (tertiary C), 127.4, 129.7, 148.5, 155.4, 157.4 ppm (quaternary C); MS (ES): m/z: 556.4 ([M^++H]).

Preparation of 2,6-bis-[5-(3,4,5-tris-dodecyloxybenzoyloxy)-1-[4-(3,4,5-tris-dodecyloxy-benzoyloxy)-benzyl]-1*H*-benzimidazol-2-yl]pyridine (L11): 2,6-Bis-(5-hydroxy-1-(4-hydroxybenzyl)-1H-benzimidazol-2-yl)pyridine (**5**, 0.27 g, 0.48 mmol), 3,4,5-tris-dodecyloxybenzoic acid (4 g, 5.93 mmol),[18] 1-(3-dimethylaminopropyl)-3-ethyl-carbodiimide hydrochloride (EDCI, 1.13 g, 5.93 mmol) and a catalytic amount of 4-dimethylaminopyridine (DMAP) were refluxed in dichloromethane/DMF (49/11 mL) for 48 h under an inert atmosphere. The resulting solution was washed with water (3×75 mL), then with half-sat aq $NaHCO_3$ (25 mL), and the organic phase was separated. The aq phase was extracted with dichloromethane (3×50 mL) and the combined organic phases were dried (Na_2SO_4) and the solvent evaporated. The crude residue was purified by column chromatography (silica gel; CH_2Cl_2/AcOEt 98:2→96:4) to give 1.08 g (0.34 mmol, yield 71%) of **L11** as a white vitreous compound. T_c 55 °C; ^{1}H NMR ($CDCl_3$): $\delta=0.84$ (m, 36H; CH_3-$C_{11}H_{22}O$), 1.22 (m, 216H; CH_3-C_9H_{18}-C_2H_4O), 1.79 (m, 24H; $C_{10}H_{21}$-CH_2-CH_2O), 4.02 (m, 24H; $C_{11}H_{23}$-CH_2O), 5.56 (s, 4H; phenyl-CH_2-N), 6.88 (d, $^3J=8.7$ Hz, 4H; H^{phenyl}), 6.97 (d, $^3J=8.7$ Hz, 4H; H^{phenyl}), 7.11 (dd, $^3J=9$ Hz, $^4J=$ 2.1 Hz, 2H; H^{bzim}), 7.33 (s, 4H; H^{phenyl}), 7.36 (d, $^3J=9$ Hz, 2H; H^{bzim}), 7.42 (s, 4H; H^{phenyl}), 7.66 (d, $^4J=2.1$ Hz, 2H; H^{bzim}), 8.01 (t, $^3J=7.8$ Hz, 1H; H^{py}), 8.34 ppm (d, $^3J=7.8$ Hz, 2H; H^{py}); ^{13}C NMR ($CDCl_3$): $\delta=14.3$ (primary C); 22.9, 26.3, 29.5, 29.6, 29.6, 29.9, 29.9, 29.9, 30.5, 32.1, 69.5, 73.8 (secondary C); 108.7, 108.8, 111.4, 113.3 118.9, 122.5, 126.1, 127.6 (tertiary C); 123.8, 124.2, 134.8, 134.9, 138.5, 143.1, 143.2, 147.4, 149.6, 150.6, 151.2, 153.2, 165.2, 165.7 ppm (quaternary C); MS (ESI) (CH_2Cl_2): m/z: 1593.72 ([M+2H^{2+}]); elemental analysis calcd (%) for $C_{205}H_{329}N_5O_{20}{\cdot}1\,H_2O$: C 76.91, H 10.42, N 2.19; found: C 76.91, H 10.25, N 2.09.

Preparation of 2,6-bis-[5-(4-ethoxybenzoyloxy)-1-[4-(4-ethoxybenzoyloxy)benzyl]-1*H*-benzimidazol-2-yl]pyridine (L12): The same procedure as that described for **L11** was followed with 4-ethoxybenzoic acid instead of 3,4,5-tris-dodecyloxybenzoic acid, in order to give 97% of **L12**. ^{1}H NMR ($CDCl_3$): $\delta_H=1.42$–1.47 (q, 12H), 4.07–4.15 (sext, 8H), 5.57 (s, 4H), 6.91–7.02 (m, 16H), 7.14–7.17 (dd, $^3J=8{,}84$ Hz, $^4J=2.03$ Hz, 2H), 7.39–7.41 (d, $^3J=8{,}85$ Hz, 2H), 7.70 (d, $^4J=2.02$ Hz, 2H), 8.02–8.06 (t,

$^3J = 8.09$ Hz, 1H), 8.09–8.11 (d, $^3J = 9.09$ Hz, 4H), 8.17–8.19 (d, $^3J = 8.85$ Hz, 4H), 8.36–8.38 ppm (d, $^3J = 8.08$ Hz, 2H); MS (ESI) (CH_2Cl_2): m/z: 1448.7 ([M^++H]).

Preparation of the complexes [Ln(L11)$(NO_3)_3$] (Ln = La–Lu, Y; 6–15): Ligand **L11** (0.1 g, 0.0314 mmol) and $Ln(NO_3)_3{\cdot}xH_2O$ (Ln = La–Lu, Y; $x = 2$–4, 0.0314 mmol) were stirred in acetonitrile/dichloromethane (5:5 mL) for 1 h. After cooling to −30 °C for 12 h, the white precipitate was separated by filtration, washed with acetonitrile and dried to give 63–88 % of [Ln(**L11**)$(NO_3)_3$]·xH_2O (Ln: La, $x = 1.6$: **6;** Ln: Pr, $x = 0.5$: **7;** Ln: Sm, $x = 1.8$: **8;** Ln: Eu, $x = 1.6$: **9;** Ln: Gd, $x = 1.0$: **10;** Ln: Tb, $x = 0$: **11;** Ln: Tm, $x = 0$: **12;** Ln: Yb, $x = 0$: **13;** Ln: Lu, $x = 0$: **14;** Ln: Y, $x = 0$: **15**). All the complexes were characterized by IR spectra and by undergoing elemental analyses (see Table S1 in the Supporting Information), which agreed with TGA analyses.

Preparation of the complexes [Eu(L11)$(CF_3CO_2)_3$] (16) and [Ln(L12)-$(CF_3CO_2)_3$] (Ln = Eu, 17; Ln = Lu, 18): Ligand **L11** (0.1 g, 0.0314 mmol) and $Eu(CF_3CO_2)_3{\cdot}3H_2O$ (34.3 mg, 0.0628 mmol) were stirred in acetonitrile/dichloromethane (5:5 mL) for 1 h. After cooling to −30 °C for 12 h, the white precipitate was separated by filtration, carefully washed with acetonitrile and dried to give 84 % of [Eu(**L11**)-$(CF_3CO_2)_3$] (**16**). All the complexes were characterized by IR spectra and by satisfying elemental analyses (see Table S1 in the Supporting Information), which agree with TGA analyses. The same procedure was use for the preparation of [Ln(**L12**)$(CF_3CO_2)_3$]·xH_2O (Ln = Eu, $x = 3.9$: **17;** Ln = Lu, $x = 0.5$: **18)**. The latter complex could be recrystallized upon slow evaporation of a concentrated dichloromethane solution to give colorless prisms suitable for an X-ray diffraction investigation.

Single-crystal structure determinations: Summary of crystal data, intensity measurements and structure refinements for [Lu(**L12**)$(CF_3CO_2)_3]_2{\cdot}H_2O$ (**18**) are collected in Table 5. The crystal was mounted on quartz fibers with protection oil. Cell dimensions and intensities were measured at 200 K on a Stoe IPDS diffractometer with graphite-monochromated $Mo_{K\alpha}$ radiation ($\lambda = 0.71073$ Å). Data were corrected for Lorentz and polarization effects and for absorption. The structure was solved by direct methods (SIR97),[43] all other calculations were performed with the XTAL[44] system and ORTEP[45] programs. CCDC-637970 contains the supplementary crystallographic data for **18**. These data can be obtained free of charge from the Cambridge Crystallographic Data Centre via www.ccdc.cam.ac.uk/data_request/cif. The four ethoxy groups and one aromatic side arm (C12–C33) were disordered and refined with restraints. The disordered aromatic side arm was refined on two sites with population parameters of 0.6 and 0.4. The atomic positions of the hydrogen atoms were calculated.

Table 5. Summary of crystal data, intensity measurement and structure refinement for [Lu(**L12**)$(CF_3CO_2)_3]_2$ (**18**).

formula	$C_{150}H_{116}F_{18}Lu_2N_{10}O_{32}$
Fw	3342.6
crystal system	monoclinic
space group	$P2_1/c$ (no 14)
a [Å]	20.6423 (10)
b [Å]	19.6447 (10)
c [Å]	19.0406 (8)
α [°]	90
β [°]	100.014 (6)
γ [°]	90
V [Å^3]	7603.6 (6)
Z	2
crystal size [mm]	$0.074 \times 0.18 \times 0.32$
ρ_{calcd} [g cm^{-3}]	1.460
$\mu(Mo_{K\alpha})$ [mm^{-1}]	1.392
T_{min}, T_{max}	0.7413, 0.9019
$2\theta_{max}$ [°]	51.8
no of reflns collected	76153
no of independent reflns	14793
criterion (q) for obsd reflns[a],[b]	4
no of obsd[a] (used[b]) reflns	7177 (7558)
no of variables	1053
weighting scheme p[c]	0.00012
max and min $\Delta\rho$ [e Å^{-3}]	1.50, −0.83
GOF [d] (all data)	1.36(2)
R[e], ωR[f]	0.037, 0.037

[a] $|F_o| > q\sigma(F_o)$. [b] Used in the refinements (including reflns with $|F_o| \leq q\sigma(F_o)$ if $|F_c| > |F_o|$. [c] $\omega = 1/[\sigma^2(F_o) + p(F_o)^2]$. [d] $S = [\Sigma\{((F_o - F_c)/\sigma(F_o))^2\}/(N_{ref} - N_{var})]^{1/2}$. [e] $R = \Sigma||F_o| - |F_c||/\Sigma|F_o|$. [f] $\omega R = [\Sigma(\omega|F_o| - |F_c|/\Sigma\omega|F_o|^2]^{1/2}$.

Spectroscopic and analytical measurements: Electronic spectra in the UV/Vis were recorded at 20 °C from solutions in CH_3CN/CH_2Cl_2 (1:1) by using a Perkin–Elmer Lambda 900 spectrometer by using quartz cells of 0.1- or 1 mm-path-length. Spectrophotometric titrations were performed with a J&M diode array spectrometer (Tidas series) connected to an external computer. In a typical experiment, **L11** (50 mL) in CH_3CN/CH_2Cl_2 (1/1, 10^{-4} mol dm^{-3}) was titrated at 20 °C with a solution of $Ln(NO_3)_3{\cdot}xH_2O$ (10^{-3} mol dm^{-3}) in the same solvent under an inert atmosphere. After each addition of 0.10 mL, the absorbance was recorded by using Hellma optrodes (optical path length 0.1 cm) immersed in the thermostated titration vessel and connected to the spectrometer. Mathematical treatment of the spectrophotometric data was performed with factor analysis[46] and with the SPECFIT program.[35] IR spectra were obtained by using KBr pellets with a Perkin–Elmer Spectrum One FTIR instrument. ^{1}H and ^{13}C NMR spectra were recorded at 25 °C on Bruker Avance 400 MHz and Bruker DRX-500 MHz spectrometers. Chemical shifts are given in ppm with respect to TMS. Pneumatically-assisted electrospray (ESIMS) mass spectra were recorded from 10^{-4} mol dm^{-3} solutions by using a Finnigan SSQ7000 instrument. The equipment and experimental procedures for luminescence measurements in the visible range were published previously.[47] Excitation of the finely powdered samples was achieved by a 300 W xenon high-pressure lamp coupled with a monochromator or a Coherent Innova Argon laser. The emitted light was analyzed at 90° with a Spex 1404 double monochromator with holographic gratings (bandpass used 0.01–0.2 nm). Emitted photon flux was measured with a Hamatsu R-943–02 photomultiplier with a cooled CaAs(Cs) photocathode (−20 °C), coupled to a home-built linear amplifier (440 MHz) and a Stanford Research SR-400 double-photon counter. The emission spectra were corrected for the instrumental response. Luminescent lifetimes were measured by using excitation provided by a Quantum Brillant Nd:YAG laser equipped with frequency doubler, tripler, and quadrupler, as well as, with an OPOTEK MagicPrism OPO crystal. Selective excitations of the 0–0 profiles were performed by means of a Continuum MD 6000 dye laser pumped at 532 nm. The output signal of the photomultiplier was fed into a Stanford Research SR-430 multichannel scaler and transferred to a PC. Lifetimes were averages of three independent determinations. Quantum yields were determined using a Perkin–Elmer LS50B fluorimeter. The quantum yields were calculated by using the equation $\frac{\Phi_x}{\Phi_r} = \frac{A_r(\tilde{\nu})\cdot I_r(\tilde{\nu})\cdot n_x^2\cdot D_x}{A_x(\tilde{\nu})\cdot I_x(\tilde{\nu})\cdot n_r^2\cdot D_r}$, where x refers to the sample and r to the reference; A is the absorbance, $\tilde{\nu}$ the excitation wavenumber used, I the intensity of the excitation light at this energy, n the refractive index ($n = 1.341$ for acetonitrile solution and $n = 1.334$ for 0.1 mol dm^{-3} aq tris-buffer solution) and D the integrated emitted intensity. Cs_3[Eu(2,6-pyridine-dicarboxylic acid)$_3$] ($\varphi = 24 \pm 2.5$ % in 0.1 mol dm^{-3} aq tris-buffer solution) and Cs_3[Tb(2,6-pyridine-dicarboxylic acid)$_3$] ($\varphi = 22 \pm 2.5$ % in 0.1 mol dm^{-3} aq tris-buffer solution) were used as reference.[37] Thermogravimetric (TG) measurements were performed with a TG balance Seiko TG/DTA 320 (under N_2). DSC traces were obtained with a Seiko DSC 220C differential scanning calorimeter from 3–5 mg samples (5 °C min^{-1}, under N_2). The characterization of the mesophases was performed with a polarizing microscope Leitz Orthoplan-Pol with a Leitz LL 20x/0.40 polarizing objective, and equipped with a Linkam THMS 600 variable-temperature stage. The SAXS patterns were obtained with four different experimental setups, and in all cases, the crude powder was filled in Lindemann capillaries of 1 mm diameter. Diffraction patterns (laboratory source) were measured with three different instruments: 1) a STOE transmission powder diffractometer system STADI P by using a focused monochromatic $Cu_{K\alpha 1}$ beam obtained from a curved Germanium monochromator (Johann-type) and collected on a curved Image-Plate Position-Sensitive Detector (IP-PSD). A calibration with silicon and copper laurate stand-

ards, for high- and low-angle domains respectively, was initially performed. Sample capillaries were placed in the high-temperature attachment for measurements in the range of desired temperatures (from −40 up to 170 °C) within ±0.05 °C. Periodicities up to 50 Å could be measured. The exposure times were varied from 1 to 4 h. 2) A curved counter Inel CPS 120 by using a linear monochromatic $Cu_{K\alpha 1}$ beam obtained with a sealed-tube generator (900 W) and a bent quartz monochromator, for which the sample temperature was controlled within ±0.05 °C; periodicities up to 60 Å could be measured. 3) An Image Plate; the cell parameters were calculated from the position of the reflection at the smallest Bragg angle, which was in all cases the most intense. Periodicities up to 90 Å could be measured, and the sample temperature was controlled within ±0.3 °C. The exposure times were varied from 1 to 24 h depending on the specific reflections being sought (weaker reflections obviously taking longer exposure times). Diffraction patterns (SLS) were measured by using the synchrotron radiation Swiss Light Source (SLS) at the Paul Scherrer Institut (PSI), Villigen, Switzerland. Measurements were performed at the material science (MS) beamline by using the wavelengths $\lambda = 0.4328$ or 0.87943 Å (depending on the sample). The microstrip detector, covering an angular range of 60°, allows extremely fast in-situ measurements depending on the temperature (around 50–80 s per temperature step) which prevents the decomposition of these fragile complexes under heating, and give reliable structural data to complete the DSC and polarized light microscopy (PLM) measurements. Moreover, the high signal/noise ratio allows the detection of weak Bragg peaks and leads to a more accurate indexation for some poorly organized phases. Elemental analyses were performed by Dr. H. Eder from the microchemical Laboratory of the University of Geneva.

Acknowledgements

We thank K. Buchwalder for her technical assistance. B.D. and D.G. thank the CNRS-Université Louis Pasteur for support. L.G. thanks Dr. B. Schmitt and Dr. F. Gozzo from SLS-MS beamline at PSI, Villigen, for their help with the synchrotron diffraction experiments. Financial support from the Swiss National Science Foundation is gratefully acknowledged.

[1] K. Binnemans, C. Görller-Walrand, *Chem. Rev.* **2002**, *102*, 2303–2346.

[2] a) C. Piechocki, J. Simon, J. J. André, D. Guillon, P. Petit, A. Skoulios, P. Weber, *Chem. Phys. Lett.* **1985**, *122*, 124–128; b) T. Komatsu, K. Ohta, T. Fujimoto, I. Yamamoto, *J. Mater. Chem.* **1994**, *4*, 533–536; c) T. Toupance, P. Bassoul, L. Mineau, J. Simon, *J. Phys. Chem.* **1996**, *100*, 11704–11710; d) K. Ban, K. Nishizawa, K. Ohta, A. Van de Craats, J. M. Warman, I. Yamamoto, H. Shirai, *J. Mater. Chem.* **2001**, *11*, 321–331; e) J. Sleven, C. Görller-Walrand, K. Binnemans, *Mater. Sci. Eng. C* **2001**, *9*, 229–238; f) F. Maeda, K. Hatsusaka, K. Ohta, M. Kimura, *J. Mater. Chem.* **2003**, *13*, 243–251; g) K. Binnemans, J. Sleven, S. De Feyter, F. C. De Schryver, B. Donnio, D. Guillon, *Chem. Mater.* **2003**, *15*, 3930–3938.

[3] H. Miwa, N. Kobayashi, K. Ban, K. Ohta, *Bull. Chem. Soc. Jpn.* **1999**, *72*, 2719–2728.

[4] a) I. V. Ovchinnikov, Y. G. Galyametdinov, G. I. Ivanova, L. M. Yagfarova, *Dokl Akad Nauk SSSR* **1984**, *276*, 126–128; b) Y. G. Galyametdinov, I. V. Ovchinnikov, B. M. Bolotin, N. B. Etingen, G. I. Ivanova, L. M. Yagarova, *Izv Akad Nauk SSSR, Ser Khim* **1984**, 2379–2381; c) Y. G. Galyametdinov, D. Z. Zakieva, I. V. Ovchinnikov, *Izv. Akad. Nauk Gruz. SSR Ser. Khim.* **1986**, 491; d) I. V. Ovchinnikov, I. G. Galyametdinov, I. G. Bikchantaev, *Izv. Akad. Nauk Kaz. SSR Ser. Fiziol.* **1989**, *53*, 1870–1879; e) R. M. Galimov, I. G. Bikchantaev, I. V. Ovchinnikov, *Zh Strukt Khim* **1989**, *30*, 65–69; f) Y. G. Galyametdinov, M. A. Athanassopoulou, K. Griesar, O. Kharitonova, E. A. Soto Bustamante, L. Tinchurina, I. V. Ovchinnikov, W. Haase, *Chem. Mater.* **1996**, *8*, 922–926; g) K. Binnemans, Y. G. Galyametdinov, S. R. Collinson, D. W. Bruce, *J. Mater. Chem.* **1998**, *8*, 1551–1553; h) K. Binnemans, Y. G. Galyametdinov, R. Van Deun, D. W. Bruce, S. R. Collinson, A. P. Polishchuk, I. Bikchantaev, W. Haase, A. V. Prosvirin, L. Tinchurina, U. Litvinov, A. Gubajdullin, A. Rakhmatullin, K. Uytterhoeven, L. Van Meervelt, *J. Am. Chem. Soc.* **2000**, *122*, 4335–4344; i) R. Van Deun, K. Binnemans, *Liq. Cryst.* **2001**, *28*, 621–627; j) Y. G. Galyametdinov, W. Haase, L. Malykhina, A. Prosvirin, I. Bikchantaev, A. Rakhmatullin, K. Binnemans, *Chem. Eur. J.* **2001**, *7*, 99–105; k) K. Binnemans, D. Moors, T. N. Parac-Vogt, R. Van Deun, D. Hinz-Hübner, G. Meyer, *Liq. Cryst.* **2002**, *29*, 1209–1216; l) N. V. Rao, M. K. Paul, T. R. Rao, A. Prasad, *Liq. Cryst.* **2002**, *29*, 1243–1246; m) L. Van Meervelt, K. Uytterhoeven, R. van Deun, K. Binnemans, *Z. Kristallogr. New Cryst. Struct.* **2003**, *218*, 488–490.

[5] a) K. Binnemans, K. Lodewyckx, B. Donnio, D. Guillon, *Chem. Eur. J.* **2002**, *8*, 1101–1105; b) K. Binnemans, K. Lodewyckx, *Supramol. Chem.* **2003**, *15*, 485–494; c) K. Binnemans, K. Lodewyckx, B. Donnio, D. Guillon, *Eur. J. Inorg. Chem.* **2005**, 1506–1513.

[6] K. Binnemans, K. Lodewyckx, T. Cardinaels, T. N. Parac-Vogt, C. Bourgogne, D. Guillon, B. Donnio, *Eur. J. Inorg. Chem.* **2006**, 150–157.

[7] T. Cardinaels, K. Driesen, T. N. Parac-Vogt, B. Heinrich, C. Bourgogne, D. Guillon, B. Donnio, K. Binnemans, *Chem. Mater.* **2005**, *17*, 6589–6598.

[8] T. Cardinaels, J. Ramaekers, D. Guillon, B. Donnio, K. Binnemans, *J. Am. Chem. Soc.* **2005**, *127*, 17602–17603.

[9] a) S. Clark, J. M. Elliot, J. R. Chipperfield, P. M. Styring, E. Sinn, *Inorg. Chem. Commun.* **2002**, *5*, 249–251; b) J. M. Elliott, J. R. Chipperfield, S. Clark, S. J. Teat, E. Sinn, *Inorg. Chem.* **2002**, *41*, 293–299; c) J. L. Sessler, W. B. Callaway, S. P. Dudek, R. W. Date, D. W. Bruce, *Inorg. Chem.* **2004**, *43*, 6650–6653; d) I. Aiello, M. Ghedini, A. Grisolia, D. Pucci, O. Francescangeli, *Liq. Cryst.*, **2005**, *32*, 763–769; e) J. L. Sessler, P. J. Melfi, E. Tomat, W. Callaway, M. T. Huggins, P. L. Gordon, K. D. Webster, R. W. Date, D. W. Bruce, B. Donnio, *J. Alloys Compds* **2006**, *418*, 171–177.

[10] a) E. Terazzi, S. Suarez, S. Torelli, H. Nozary, D. Imbert, O. Mamula, J.-P. Rivera, E. Guillet, J.-M. Bénech, G. Bernardinelli, R. Scopelliti, B. Donnio, D. Guillon, J.-C. G. Bünzli, C. Piguet, *Adv. Funct. Mater.* **2006**, *16*, 157–168; b) C. Piguet, J.-C. G. Bünzli, B. Donnio, D. Guillon, *Chem. Commun.* **2006**, 3755–3768.

[11] A. A. Levchenko, C. K. Yee, A. N. Parikh, A. Navrotsky, *Chem. Mater.* **2005**, *17*, 5428–5438.

[12] a) M. S. Searle, D. H. Williams, *J. Am. Chem. Soc.* **1992**, *114*, 10690–10697; b) M. S. Searle, M. S. Westwell, D. H. Williams, *J. Chem. Soc. Perkin Trans. 2* **1995**, 141–151; c) D. H. Williams, D. P. O'Brien, B. Bardsley, *J. Am. Chem. Soc.* **2001**, *123*, 737–738.

[13] D. M. Ford, *J. Am. Chem. Soc.* **2005**, *127*, 16167–16170.

[14] E. Terazzi, L. Guénée, P.-Y. Morgantini, G. Bernardinelli, B. Donnio, D. Guillon, C. Piguet, *Chem. Eur. J.* **2007**, *13*, 1674–1691.

[15] H. Nozary, C. Piguet, P. Tissot, G. Bernardinelli, J.-C. G. Bünzli, R. Deschenaux, D. Guillon, *J. Am. Chem. Soc.* **1998**, *120*, 12274–12288.

[16] H. Nozary, C. Piguet, J.-P. Rivera, P. Tissot, G. Bernardinelli, N. Vulliermet, J. Weber, J.-C. G. Bünzli, *Inorg. Chem.* **2000**, *39*, 5286–5298.

[17] H. Nozary, C. Piguet, J.-P. Rivera, P. Tissot, P.-Y. Morgantini, J. Weber, G. Bernardinelli, J.-C. G. Bünzli, R. Deschenaux, B. Donnio, D Guillon, *Chem. Mater.* **2002**, *14*, 1075–1090.

[18] a) E. Terazzi, J.-M. Bénech, J.-P. Rivera, G. Bernardinelli, B. Donnio, D. Guillon, C. Piguet, *Dalton Trans.* **2003**, 769–772; b) E. Terazzi, S. Torelli, G. Bernardinelli, J.-P. Rivera, J.-M. Bénech, C. Bourgogne, B. Donnio, D. Guillon, D. Imbert, J.-C. G. Bünzli, A. Pinto, D. Jeannerat, C. Piguet, *J. Am. Chem. Soc.* **2005**, *127*, 888–903.

[19] H. Nozary, S. Torelli, L. Guénée, E. Terazzi, G. Bernardinelli, B. Donnio, D. Guillon, C. Piguet, *Inorg. Chem.* **2006**, *45*, 2989–3003.

[20] a) K. Nakamoto, *Infrared and Raman Spectra of Inorganic and Coordination Compounds*, 5th ed., Part B, Wiley, New York, **1997**, pp. 87–89; b) C. Piguet, A. F. Williams, G. Bernardinelli, E. Moret, J.-C. G. Bünzli, *Helv. Chim. Acta* **1992**, *75*, 1697–1717.

[21] R. D. Shannon, *Acta Crystallogr. Sect. A* **1976**, *32*, 751–767.

[22] C. Piguet, J.-C. G. Bünzli, G. Bernardinelli, C. G. Bochet, P. Froidevaux, *J. Chem. Soc. Dalton Trans.* **1995**, 83–97.

[23] a) S. Tobita, M. Arakawa, I. Tanaka, *J. Phys. Chem.* **1984**, *88*, 2697–2702; b) S. Tobita, M. Arakawa, I. Tanaka, *J. Phys. Chem.* **1985**, *89*, 5649–5654.
[24] a) N. Sabbatini, M. Guardigli, I. Manet in *Handbook on the Physics and Chemistry of Rare Earths, Vol. 23* (Eds.: K. A. Gschneidner, L. Eyring) Elsevier, Amsterdam, **1996**, pp. 69–120; b) J.-C. G. Bünzli, C. Piguet, *Chem. Soc. Rev.* **2005**, *34*, 1048–1077.
[25] S. T. Frey, W. de W. Horrocks, *Inorg. Chim. Acta* **1995**, *228*, 383–390.
[26] a) C. Piguet, E. Rivara-Minten, G. Hopfgartner, J.-C. G. Bünzli, *Helv. Chim. Acta* **1995**, *78*, 1541–1566; b) C. Piguet, J.-C. G. Bünzli, G. Bernardinelli, G. Hopfgartner, S. Petoud, O. Schaad, *J. Am. Chem. Soc.* **1996**, *118*, 6681–6697.
[27] J.-C. G. Bünzli, in *Lanthanide Probes in Life, Chemical and Earth Sciences* (Eds.: J.-C. G. Bünzli, and G. R. Choppin), Elsevier Publishing Co., Amsterdam, **1989**, Chapter 7.
[28] a) W. de W. Horrocks, D. R. Sudnick, *J. Am. Chem. Soc.* **1979**, *101*, 334–340; b) W. de W. Horrocks, D. R. Sudnick, *Acc. Chem. Res.* **1981**, *14*, 384–392; c) A. Beeby, I. M. Clarkson, R. S. Dickins, S. Faulkner, D. Parker, L. Royle, A. S. de Sousa, J. A. G. Williams, M. Woods, *J. Chem. Soc. Perkin Trans. 2* **1999**, 493–503; d) I. Billard, in *Handbook on the Physics and Chemistry of Rare Earths, Vol. 33* (Eds.: K. A. Gschneidner Jr., J.-C. G. Bünzli, V. K. Pecharsky), Elsevier Science, Amsterdam, **2003**, pp. 465–514.
[29] a) D. W. Bruce, B. Donnio, S. A. Hudson, A.-M. Levelut, S. Megtert, D. Peterman, M. Veber, *J. Phys. II France* **1995**, *5*, 289–302; b) B. Donnio, B. Heinrich, T. Gulik-Krzywicki, H. Delacroix, D. Guillon, D. W. Bruce, *Chem. Mater.* **1997**, *9*, 2951–2965; c) B. Donnio, D. W. Bruce, H. Delacroix, T. Gulik-Krzywicki, *Liq. Cryst.* **1997**, *23*, 147–153; d) B. Donnio, K. E. Rowe, C. P. Roll, D. W. Bruce, *Mol. Cryst. Liq. Cryst.* **1999**, *332*, 383–390.
[30] P. W. Atkins, *Physical Chemistry*, 5th ed., Oxford University Press, Oxford-Melbourne-Tokyo, **1994**, pp. 200–203.
[31] J. C. Tolédano, P. Tolédano, *The Landau Theory of Phase Transition*, World Scientific Publishing Co., Singapore, **1987**, pp. 166–214.
[32] a) K. Sénéchal, L. Toupet, I. Ledoux, J. Zyss, H. Le Bozec, O. Maury, *Chem. Commun.* **2004**, 2180–2181; b) K. Sénéchal-David, A. Hemeryck, N. Tancrez, L. Toupet, J. A. G. Williams, I. Ledoux, J. Zyss, A. Boucekkine, J.-P. Guégan, H. Le Bozec, O. Maury, *J. Am. Chem. Soc.* **2006**, *128*, 12243–12255; c) N. Tancrez, C. Feuvrie, I. Ledoux, J. Zyss, L. Toupet, H. Le Bozec, O. Maury, *J. Am. Chem. Soc.* **2005**, *127*, 13474–13475.
[33] a) S. Suarez, O. Mamula, D. Imbert, C. Piguet, J.-C. G. Bünzli, *Chem. Commun.* **2003**, 1226–1227; b) S. Suarez, D. Imbert, F. Gumy, C. Piguet, J.-C. G. Bünzli, *Chem. Mater.* **2004**, *16*, 3257–3266; c) K. Driesen, K. Binnemans, *Liq. Cryst.* **2004**, *31*, 601–605.
[34] a) M. Kleinerman, S.-I. Choi *J. Chem. Phys.* **1968**, *49*, 3901–3910; b) S. Hüfner, *Optical Spectra of Transparent Rare Earth Compounds*, Academic Press, New York, **1978**.
[35] a) H. Gampp, M. Maeder, C. J. Meyer, A. Zuberbühler, *Talanta*, **1985**, *32*, 1133–1139; b) H. Gampp, M. Maeder, C. J. Meyer, A. Zuberbühler, *Talanta* **1986**, *33*, 943–951.
[36] C. Piguet, J.-C. G. Bünzli, G. Bernardinelli, A. F. Williams, *Inorg. Chem.* **1993**, *32*, 4139–4149.
[37] A.-S. Chauvin, F. Gumy, D. Imbert, J.-C. G. Bünzli, *Spectrosc. Lett.* **2004**, *37*, 517–532; A.-S. Chauvin, F. Gumy, D. Imbert, J.-C. G. Bünzli, *Spectrosc. Lett.* **2007**, *40*, 193.
[38] F. J. Steemers, W. Verboom, D. N. Reinhoudt, E. B. Vandertol, J. W. Verhoeven, *J. Am. Chem. Soc.* **1995**, *117*, 9408–9418.
[39] M. Latva, H. Takalo, V. M. Mukkala, C. Matachescu, J.-C. Rodriguez-Ubis, J. Kankare, *J. Lumin.* **1997**, *75*, 149–169.
[40] J. F. Desreux in *Lanthanide Probes in Life, Chemical and Earth Sciences*, Elsevier, Amsterdam, **1989**, Chapter 2.
[41] J.-C. G. Bünzli, E. Moret, J.-R. Yersin, *Helv. Chim. Acta* **1978**, *61*, 762–771.
[42] G. Schwarzenbach, *Complexometric Titrations*; Chapman & Hall, London, **1957,** pp. 8.
[43] A. Altomare, M. C. Burla, M. Camalli, G. Cascarano, C. Giacovazzo, A. Guagliardi, G. Moliterni, G. Polidori, R. Spagna, *J. Appl. Crystallogr.* **1999**, *32*, 115–119.
[44] XTAL 3.2, User's Manual (Eds.: S. R. Hall, H. D. Flack, J. M. Stewart), Universities of Western Australia and Maryland, **1989**.
[45] C. K. Johnson, ORTEP II, Report ORNL-5138, Oak Ridge National Laboratory, Oak Ridge, Tennessee, **1976**.
[46] E. R. Malinowski, D. G. Howery, *Factor Analysis in Chemistry*, Wiley, New York, Chichester, **1980**.
[47] R. Rodriguez-Cortinas, F. Avecilla, C. Platas-Iglesias, D. Imbert, J.-C. G. Bünzli, A. de Blas, T. Rodriguez-Blas, *Inorg. Chem.* **2002**, *41*, 5336–5349.

Received: April 10, 2007
Published online: July 30, 2007

